

New Gravitational Wave Discoveries Enabled by Machine Learning

Alexandra E. Koloniari,¹ Evdokia C. Koursoumpa,¹ Paraskevi Nousi,² Paraskevas Lampropoulos,¹ Nikolaos Passalis,³ Anastasios Tefas,³ and Nikolaos Stergioulas¹

¹*Department of Physics, Aristotle University of Thessaloniki, 54124 Thessaloniki, Greece*

²*Swiss Data Science Center, ETH, Zürich, Switzerland*

³*Department of Informatics, Aristotle University of Thessaloniki, 54124 Thessaloniki, Greece*

(Dated: July 11, 2024)

The detection of gravitational waves has revolutionized our understanding of the universe, offering unprecedented insights into its dynamics. A major goal of gravitational wave data analysis is to speed up the detection and parameter estimation process using machine learning techniques, in light of an anticipated surge in detected events that would render traditional methods impractical. Here, we present the first detections of new gravitational-wave candidate events in data from a network of interferometric detectors enabled by machine learning. We discuss several new enhancements of our ResNet-based deep learning code, AresGW, that increased its sensitivity, including a new hierarchical classification of triggers, based on different noise and frequency filters. The enhancements resulted in a significant reduction in the false alarm rate, allowing AresGW to surpass traditional pipelines in the number of detected events in its effective training range (single source masses between 7 and 50 solar masses and source chirp masses between 10 and 40 solar masses), when the new detections are included. We calculate the astrophysical significance of events detected with AresGW using a logarithmic ranking statistic and injections into O3 data. Furthermore, we present spectrograms, parameter estimation, and reconstruction in the time domain for our new candidate events and discuss the distribution of their properties. In addition, the AresGW code exhibited very good performance when tested across various two-detector setups and on observational data from the O1 and O2 observing periods. Our findings underscore the remarkable potential of AresGW as a fast and sensitive detection algorithm for gravitational-wave astronomy, paving the way for a larger number of future discoveries.

PACS numbers: 04.30.-w,95.30.Sf,95.85.Sz

I. INTRODUCTION

The cosmos whispers its secrets through gravitational waves, subtle ripples in the fabric of spacetime that carry profound insights into the universe's most enigmatic phenomena. In the quest to decipher these cosmic murmurs, the convergence of machine learning (ML) algorithms and gravitational wave astronomy has ushered in a new era of discovery, promising unprecedented sensitivity and efficiency in detecting these elusive signals.

During the initial three observing runs (O1-O3) conducted initially by the LIGO-Virgo Collaboration [1, 2], with the later addition of Kagra [3], around 90 gravitational wave (GW) events were confidently identified and published in the GWTC catalogs [4–7]. These events primarily consisted of binary black hole (BBH) mergers, alongside a minority of binary neutron star (BNS) and neutron star-black hole (NSBH) systems. Additional events were published in the OGC catalogs [8–11] and the IAS catalogs [12–14] and updated significance of events was discussed with the pycbc.KDE pipeline in [15]. As we find ourselves in the middle of the fourth observing run (O4) and anticipate the dawn of upgraded or next-generation detectors, such as LIGO-India [16], Voyager [17], and Virgo nEXT, Cosmic Explorer [18], Einstein Telescope [19], and NEMO [20], the need for more efficient gravitational wave detection algorithms becomes crucial [21]. Traditional matched-filtering methods face

computational challenges for near-real-time processing, compounded by the complexities of accurately detecting systems with non-aligned spins. Unmodeled search techniques, while promising, exhibit variable sensitivity to different gravitational wave sources, necessitating further exploration, especially in light of theories beyond general relativity.

In recent years, there has been an increase in the use of machine learning approaches for the analysis of gravitational wave data (see [22–24] for reviews). The implementation of convolutional neural networks (CNN), auto-encoders, and other machine-learning methods has been investigated as an attractive solution to the problem of detecting gravitational waves (GWs), see e.g. [25–70]. In [71], a new candidate event was found with a machine-learning algorithm in a single-detector search.

In the past, it has been difficult to assess the effectiveness of such efforts in a realistic setting. For this reason, the inaugural Machine-Learning Gravitational-Wave Mock Data Challenge (MLGWSC-1) was concluded [72], establishing an objective framework to assess the sensitivity and efficiency of ML algorithms on modeled injections in both Gaussian and real O3a detector noise, compared to traditional algorithms. In [73], AresGW, the leading ML algorithm for BBH template waveform injections in real O3a noise, was detailed, demonstrating that with further enhancements, it surpassed, for the first time, the results achieved with standard configurations of traditional algorithms in a specific context. This success

was achieved for a component mass range of $7 - 50M_{\odot}$ (covering 70% of the reported events in the cumulative GWTC catalog [7]) and a relatively low false-alarm rate (FAR) as low as one per month.

Here, we present several new improvements in the AresGW algorithm and assess its performance in comparison to the existing GWTC, OGC, IAS and pycbc_KDE pipelines on O3 data. This includes the definition of a logarithmic ranking statistic, inspired by [71] and the evaluation of the astrophysical probability, p_{astro} of candidate events. Furthermore, we identify *eight new* GW candidates in the O3 data, with $p_{\text{astro}} > 0.5$ and a cumulative astrophysical probability of 5.94. This is the *first identification of new coincident events in GW searches with a network of detectors by a machine-learning-based algorithm*.

A key aspect of AresGW’s algorithm that allowed us to uncover new GW candidate events in the O3 period, is that fact that it is trained to evaluate simultaneously the time-series data of the two LIGO detectors, producing directly a single ranking statistic. In this way, the network can learn patterns, relationships, or features from the combined data of the two detectors, extracting valuable information that might not have been apparent when each detector’s data is first ranked independently of the other, as is the case in traditional searches.

The paper is organized as follows: In Section II we present the methods used in our analysis. In Section III we discuss the background model and statistics. In Section IV we discuss the foreground model and statistics and in Section V we present the calculation of the astrophysical probability. In Section VI we demonstrate the confirmation of known gravitational wave events with AresGW and in Section VII we present the new candidate events found with AresGW. The paper concludes with a discussion in Section VIII.

A. Effective Training Range

II. METHODS

In the following subsections, we will introduce the different methods we used in our analysis. Starting from the training data, we will emphasize the range of chirp mass values \mathcal{M} and other parameters in which our code AresGW was trained to detect BBH merger events. We will then describe the various enhancements that we implemented with respect to the initial version of AresGW in [73], the removal of known glitches, the parameter estimation procedure and, finally, the various consistency checks of new candidate events.

A. Training Data

The training dataset consists of real O3a noise from the two LIGO detectors, with a duration equivalent to

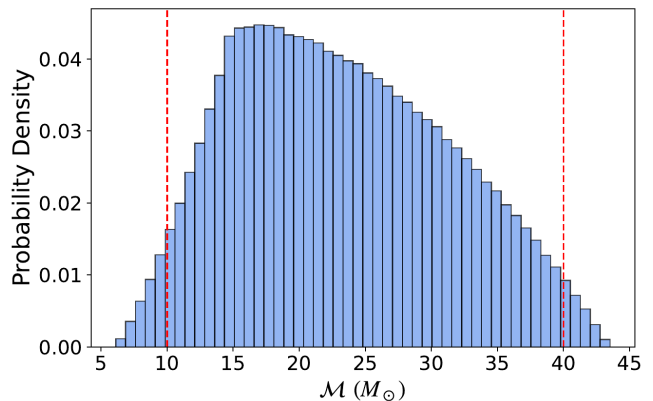


FIG. 1: Due to the relationship between the individual masses m_1 and m_2 and the chirp mass (\mathcal{M}), the resulting distribution of the chirp mass appears skewed, even though m_1 and m_2 both follow a uniform distribution. Considering the final distribution of \mathcal{M} , the probability for a modeled waveform used in training to have $\mathcal{M} < 10$ is approximately 0.027, while the probability for $\mathcal{M} > 40$ is approximately 0.017. The dashed red lines on the plot represent the \mathcal{M} values of 10 and 40. We consider only the \mathcal{M} values between those two lines to be within the training dataset range since the network hasn’t been exposed to enough samples from outside that range to be effectively trained on them.

35 days, generated with the code used in [72], with a random seed of 42 and with a start time on day 45 of the initial dataset with an equivalent duration of 81 days. This represents a significant increase in the duration of the training set, which was 12 days in our previous version of AresGW [73, 74]. Since a partial overlap of the noise used in the training with the O3 data may have a negative impact on the accuracy of the code, we mitigate this effect, by randomly shuffling 40% of the noise segments between the two detectors in each epoch, leading to only a small percentage of noise segments in the training samples that overlap with the test data.

The O3a noise was downloaded from the Gravitational Wave Open Science Center (GWOSC) [75], keeping the “data” quality flag active and requiring the internal “CBC_CAT1_VETO,” “CBC_CAT2_VETO,” “CBC_HW_INJ,” and “BURST_HW_INJ” flags inactive. Only segments with a minimum duration of 2 hours where both LIGO detectors were observing were included, while 10-second intervals around detections listed in GWTC-2 were excluded (see [72] for further details).

We injected model signals into the noise that were generated employing masses uniformly drawn in a range spanning from $7 M_{\odot}$ to $50 M_{\odot}$, spins characterized by an isotropic distribution with magnitudes ranging from 0 to 0.99, and random orientation. Additionally, the signals were uniformly distributed across coalescence phase, polarization, inclination, declination, and right

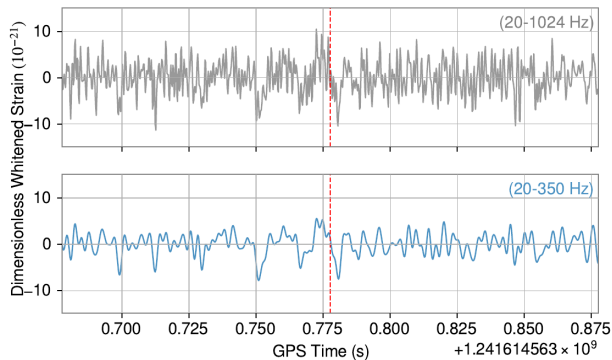


FIG. 2: An example of a time-domain segment from the Livingston detector, which includes one of the new events identified by AresGW (GW190511_135545). *Top panel:* The data is bandpassed with a 20-1024 Hz filter and appears noisy in the time domain. *Bottom panel:* With a 20-350 Hz filter the time series is less noisy, allowing for a better training of AresGW’s neural network. The red dashed line represents the merger time.

ascension, see [72, 73] for further details. The chosen waveform model, IMRPhenomXPHM [76], incorporates higher-order modes and includes precession effects.

The chirp mass distribution in the dataset used for training, as shown in Fig. 1, has a mean value of $23.2 M_{\odot}$ and a standard deviation of $8.08 M_{\odot}$. This encompasses a large fraction of the inferred distribution from published GW observations, see discussion in Section VII C. Note that although individual mass components were chosen uniformly in the range $7 M_{\odot}$ to $50 M_{\odot}$, the corresponding distribution of \mathcal{M} is nonuniform, with $\sim 95\%$ of the signals included in the range of $10M_{\odot} < \mathcal{M} < 40M_{\odot}$. We consider models outside of this range as outliers.

The justification for this is as follows: Neural networks, when trained on a dataset with a predominant distribution, tend to focus more on learning patterns within the majority of the data. In the context of a binary classification problem, where the network aims to distinguish between gravitational waves and pure noise, this means the model may become less sensitive to signals that deviate significantly from the common chirp mass values. Standard loss functions, such as mean squared error or cross-entropy, are designed to minimize errors across the entire dataset. However, when dealing with imbalanced distributions or rare events at the tails, these loss functions might not adequately penalize the misclassification of rare instances. As a result, the neural network may struggle to learn and generalize well to signals at the edges of the chirp mass distribution.

Consequently, we posit that the *effective training range* lies within $\mathcal{M} \in (10M_{\odot}, 40M_{\odot})$, acknowledging the potential limitations posed by the network’s reduced exposure to samples beyond these boundaries.

B. Enhanced AresGW Code

Our enhanced AresGW code is based on the one-dimensional ResNet structure of its previous versions [73, 74] with several critical modifications that allowed us to achieve significantly higher accuracy, that is, to better separate noise signals from signals with waveforms hidden within the noise. For instance, within the whitening module of the network, we have added a low-pass filtering mechanism alongside the existing high-pass filtering, which occurs during the inverse spectrum truncation process to compute the power spectral density. This modification is discussed in greater detail in Section II B 2.

The output of AresGW is a ranking statistic \mathcal{R} ranging from 0 to 1. For astrophysically relevant triggers, the values of \mathcal{R} are typically extremely close to 1 and we therefore follow [71] and define a logarithmic ranking statistic as

$$\mathcal{R}_s = -\log_{10}(1 - \mathcal{R}). \quad (1)$$

In this way, an exact value of $\mathcal{R} = 1$ would correspond to $\mathcal{R}_s = +\infty$. However, due to the finite precision of arithmetic operations, there exist a maximum meaningful value of \mathcal{R}_s , as we elaborate below.

1. Double precision

The network’s parameters, and every computation within it, was in single-precision floating-point format (FP32), as is typically the case for deep neural network frameworks. However, a kind of numerical underflow was observed in the output layer of the network, i.e., the final softmax function which converts the network’s predictions to a probability distribution over the two classes (noise vs. noise plus signal). Setting the entire network to double-precision floating point format (FP64) fixed the issue but at the cost of significantly increased running time (over twice the time needed with FP32). To avoid this overhead, the use of FP64 on only the final softmax layer was investigated and was found to be successful in avoiding numerical problems as well as in adding virtually zero overhead to the overall detection framework. Thus, the output of the network is converted from FP32 to FP64 before the computation of the softmax function, whose output is also in FP64 format. Note that the above change to double precision output was only implemented during deployment of the code on the O3 data. During training, only single precision was used.

Due to the algorithm’s precision extending up to 16 decimal places we make a slight modification of the definition in Eq. (1) as follows:

$$\mathcal{R}_s = -\log_{10}(1 - \mathcal{R} + 10^{-16}). \quad (2)$$

In Eq. (2), the small value of 10^{-16} was added to avoid NaN errors when \mathcal{R} was equal to 1.0 with double precision (which was the case for most of the loudest triggers).

With this choice, the maximum meaningful value of \mathcal{R}_s is 16. We emphasize that this maximum value is dependent on the above choice and represents an accumulation point of triggers that may have had even higher \mathcal{R}_s , if we had use an even higher number of digits as precision.

2. Low-pass filter in both training and data analysis

When evaluating the efficacy of our prior model [73], we observed instances where signals with moderate to low signal-to-noise ratios (SNR) were not effectively detected by the network. Upon closer inspection, we determined that the lack of detection stemmed from the presence of higher frequency noise masking the signals' waveforms. To mitigate this issue, we adopted a low-pass filter set at 350 Hz to filter out extraneous noise, thereby enhancing the "visibility" of the signals for the network. To optimize the network's performance, we used the low-pass filter on both training and O3 datasets. This decision was made to ensure improved signal detection accuracy. As illustrated in Fig. 2, we compare the effects of applying different cut-off frequencies on one of our new detections, GW190511.135545, on the Livingston detector data frame. The upper panel represents the signal with a 1024 Hz cut-off, while the lower panel depicts the signal with a 350 Hz cut-off. In the case of the 350 Hz cut-off frequency, the signal remains discernible, whereas with the 1024Hz cut-off frequency, it becomes contaminated with larger noise variations. It should be noted that this signal exhibited an SNR of 7.34 at the Livingston detector.

In this context, it is important to note that while the choice of a 350 Hz threshold for the majority of signals in our training dataset is generally effective, it may not be optimal for all cases. Specifically, the maximum frequency of signals with smaller \mathcal{M} , such as GW190925.232845, may exceed this threshold. This also holds true for signals originating from two black holes with smaller component masses, exemplified by GW191204.171526 or GW191216.213338. However, such signals lie outside the scope of our current training dataset, as elaborated in Section IA. For future searches in other mass ranges, it is likely that this threshold may need adjustment.

Despite these considerations, it appears that the neural network adeptly recognises signals resembling those mentioned, even when the low-pass filter truncates part of the signal in the frequency domain. For instance, the network successfully identifies GW191204.171526 with the highest achievable ranking statistic.

3. Hierarchical Classification of Triggers

After we obtain triggers with the default low-pass filter of 350Hz, we focus on the subset of triggers with $\mathcal{R}_s > 2$ and classify them according to a number of condi-

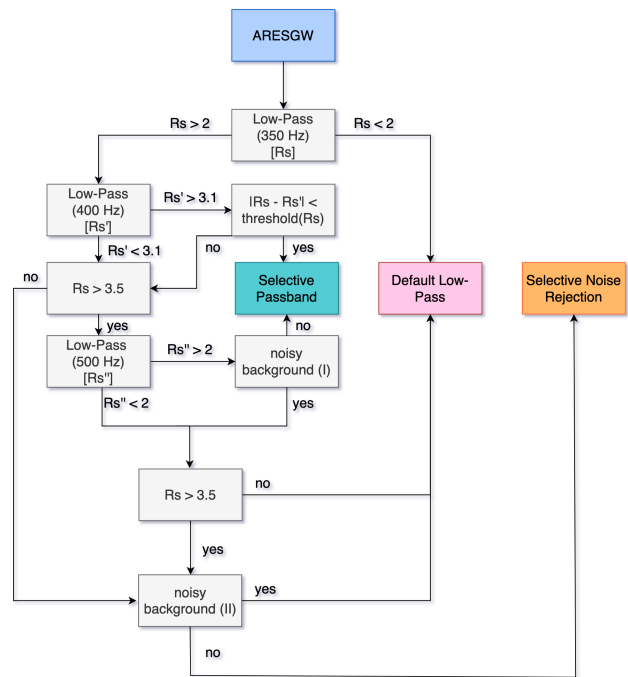


FIG. 3: Flowchart of our hierarchical classification of triggers into three different classes (see text for a detailed description)

tions, following a hierarchical scheme. This leads to three classes of triggers: a) *Default Low-Pass triggers*, b) *Selective Noise Rejection triggers*, and c) *Selective Passband triggers*. A trigger needs to satisfy certain conditions to be accepted in the Selective Noise Rejection class and even more strict conditions to be accepted in the Selective Passband class. As we will discuss in Sec. III we analyze the background statistics separately for each of these three classes and find that those belonging to the Selective Passband class have significantly lower FAR than the other two classes.

Fig. 3 describes in detail our hierarchical trigger classification scheme for triggers with $\mathcal{R}_s < 16$. In the first step, triggers with $\mathcal{R}_s < 2$ are classified as Default Low-Pass, whereas those with $\mathcal{R}_s > 2$ are examined again, using a cut-off frequency of 400 Hz. If, with this new cutoff frequency, their ranking statistic becomes $\mathcal{R}'_s > 3.1$ and the difference $|\mathcal{R}_s - \mathcal{R}'_s|$ is less than a required threshold (which depends on \mathcal{R}_s), then these triggers are classified as Selective Passband. If $|\mathcal{R}_s - \mathcal{R}'_s|$ is larger than the threshold or $\mathcal{R}'_s < 3.1$, then if $\mathcal{R}_s > 3.5$, the trigger is examined using a third cut-off frequency of 500 Hz. If its ranking statistic is then $\mathcal{R}''_s > 2$, we examine the noise triggers in its vicinity. If no noise triggers with high ranking statistic are found near the candidate trigger (with either of the cut-off frequencies), then it is classified as belonging to the Selective Passband class. Otherwise, or if $\mathcal{R}''_s < 2$, then triggers that have $\mathcal{R}_s < 3.5$ are classified as Default Low-pass. Triggers with $\mathcal{R}_s > 3.5$ or $\mathcal{R}_s < 3.5$ but with $\mathcal{R}'_s < 3.1$, are reexamined for nearby noise trig-

gers with high ranking statistics, but with a somewhat less strict condition. If they pass this test, they are classified as Selective Noise Rejection, otherwise as Default Low-Pass.

Note that, the majority of candidate triggers are reported by AresGW with the maximum possible ranking statistic of $\mathcal{R}_s = 16$ with the default cut-off frequency of 350 Hz. For these cases, we follow a simplified classification scheme, instead of the general scheme shown in Fig. 3. Specifically, we classify such triggers as Selective Passband, if in a range of 30s around the trigger there are fewer than 30 triggers with $\mathcal{R}_s > 0.3$ (i.e. $\mathcal{R} > 0.5$, which is the threshold value for a trigger to be classified as positive instead of noise). If that is not the case, such triggers are tested for the Selective Noise Rejection class and if they do not qualify, they are classified as Default Low-Pass triggers.

In the left panel of Fig. 4 we show an example of the triggers produced by AresGW within ± 15 s of a candidate trigger. When using the default cut-off frequency of 350 Hz, the candidate trigger is reported with $\mathcal{R} = 0.9999976$, which corresponds to $\mathcal{R}_s = 5.62$. When the cut-off frequency is raised to 400 Hz, the ranking statistic reduces to $\mathcal{R}'_s = 4.05$. The difference of $|5.62 - 4.05|$ is larger than the threshold value we set, which in this case is approximately 0.99. When examined with a 500 Hz cut-off frequency, the ranking statistic becomes $\mathcal{R}''_s = 2.79$. Next, the candidate trigger is rejected as belonging to either the Selective Passband or the Selective Noise Rejection classes, because of other noise triggers with high ranking statistic in its vicinity and if classified as Default Low-Pass. The right panel of Fig. 4, shows a different example, with a low-noise background, that was classified as Selective Passband.

It is important to mention that the various threshold values at the different stages of our hierarchical classification scheme were established through empirical testing and experimentation. For the Selective Noise Rejection triggers, we adjust the duration around the trigger based on the value of \mathcal{R}_s , with smaller values of \mathcal{R}_s requiring a longer time period to be examined. Signals with smaller masses tend to yield lower \mathcal{R}_s due to their morphological characteristics, such as smaller amplitudes and longer durations. It's important to note that the network evaluates one-second intervals at a time. However, the dataset's signal masses correspond to a maximum duration of 20 seconds, approximately reflecting the range of triggers checked on either side of the main trigger point for smaller \mathcal{R}_s values. Similar considerations apply to the Selective Passband triggers, where higher sensitivity for events with low \mathcal{M} is achieved by raising the low-pass cut-off frequency to 400 Hz or 500 Hz, effectively taking into account a larger part of the signal.

C. Ranking statistic optimization

In this subsection, we introduce an innovative approach based on \mathcal{R}_s , which leads to an improved calculation of the astrophysical probability p_{astro} (refer to Sec. III B). AresGW processes 1-second data segments, utilizing a 4-second window for the power spectral density (PSD) estimation. The analysis window advances in 0.1-second increments, with clustering occurring every 0.3 seconds as described in [73]. Consequently, an event can be detected by the network at any point within this 1-second data window.

This variability in an event's position within the data frame is crucial because it influences the ranking statistic generated by the network. Several factors contribute to this effect. For instance, a significant portion of an event could be truncated, or variations in the start time of the 1-second window can alter the PSD, thus changing the network's input. As a result, the event may yield different ranking statistics depending on the start time of the data frame. This principle applies equally to background noise triggers, affecting their \mathcal{R}_s values as well.

To account for the variance in \mathcal{R}_s , we define the *ensemble-averaged* $\langle \mathcal{R}_s \rangle$ in the following way. The start time shift for each trigger was applied beginning 5 seconds before the coalescence time for events and 5 seconds before the trigger time for background noise triggers. The shift step for the start time of the dataset was 0.001 seconds. The outcome of this process is illustrated in Fig. 5. It is evident that the \mathcal{R}_s values for the event GW190413.05295 (depicted in light blue) are substantially higher compared to those of the background trigger (depicted in pink). Additionally, one can observe that the \mathcal{R}_s values for the event fall within the range $[5.37, 16.0]$, highlighting the variability in the network's output for the same event. This fact underscores the unfairness of considering only the \mathcal{R}_s value from a single run, whereas using the ensemble-averaged $\langle \mathcal{R}_s \rangle$ effectively mitigates this kind of randomness.

Why is this information important? Our analysis demonstrates that, statistically, the mean of all the possible ranking statistic values for astrophysical events is significantly higher than that for noise triggers. This distinction is displayed in Fig. 6, where the light blue histogram shows the distribution of the $\langle \mathcal{R}_s \rangle$ values for all events¹, while the pink histogram represents the same for all background noise triggers. The mean of the $\langle \mathcal{R}_s \rangle$ values for all events is 10.6, compared to 4.1 for all background noise triggers.

The rationale for using the ensemble-averaged $\langle \mathcal{R}_s \rangle$ values is based on the direct relationship between the ranking statistic and the network's confidence in identifying a trigger as an event. By constructing $\langle \mathcal{R}_s \rangle$, we

¹ Here, we include all previously published events that AresGW detects with $\langle \mathcal{R}_s \rangle > 3$ and our new candidate events in Table VII with $p_{\text{astro}} \geq 0.5$.

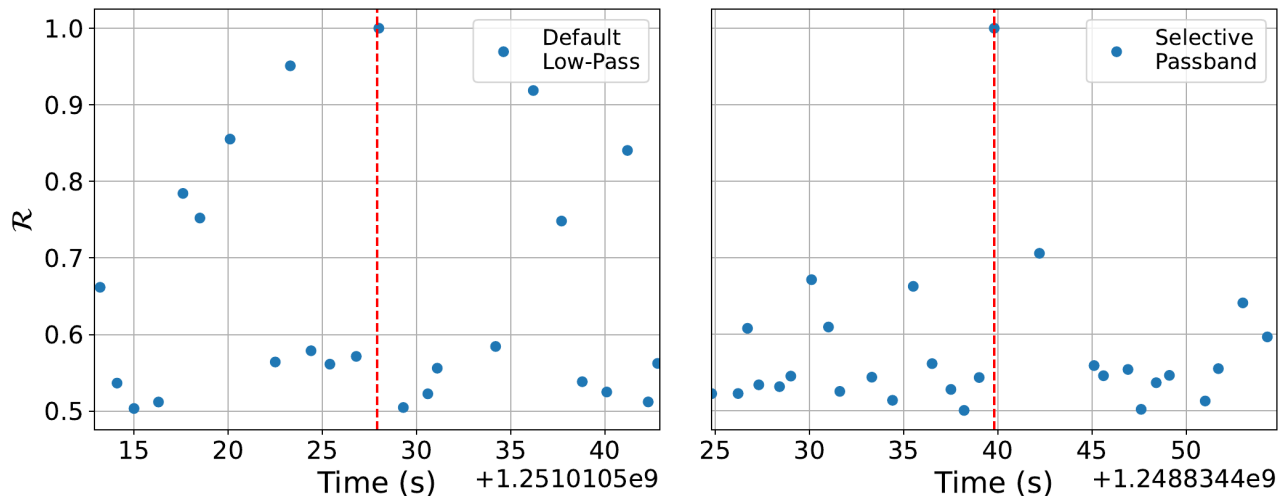


FIG. 4: *Left panel:* Ranking statistic $\mathcal{R} > 0.5$ of triggers in a time range of ± 15 s around the GWTC-3 event GW190828.065509. Due to an excessive number of noise triggers with high ranking statistic, the trigger of the candidate event is classified as Default Low-pass. *Right panel:* Same as left panel, but for the GWTC-3 event GW190828.063405. This trigger is classified as Selective Passband, due to the absence of nearby noise triggers with high ranking statistic and the fact that it still has high \mathcal{R} values for different low cutoffs.

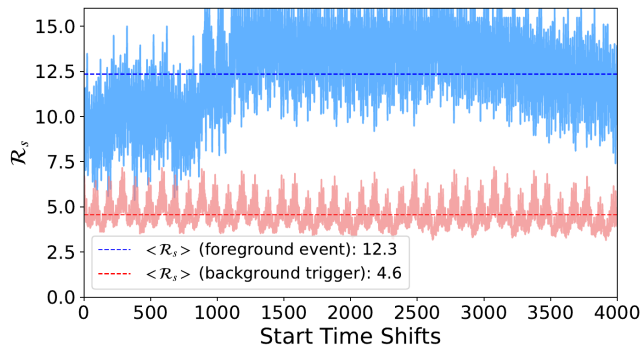


FIG. 5: Ranking statistic \mathcal{R}_s (light blue) obtained for different start times close the event GW190413.052954. In addition, we show \mathcal{R}_s for a representative noise trigger (see text for details). The blue and red dashed lines represent the ensemble-averaged values $\langle \mathcal{R}_s \rangle$, respectively.

effectively aggregate the network’s predictions across different start times, yielding a more robust and comprehensive assessment of the signal by considering it in all possible positions, with a chosen timestep, within the data frame. This approach appears to be a better criterion than the initial \mathcal{R}_s , likely because it leads to a more accurate representation of the trigger’s significance. In fact, this method appears to be particularly critical for threshold events, as demonstrated by the data: with the initial \mathcal{R}_s , AresGW would have detected 38 events within its effective training range. In contrast, using the ensemble-averaged $\langle \mathcal{R}_s \rangle$ values, it detects 42 events. The additional four events represent new near-threshold detections.

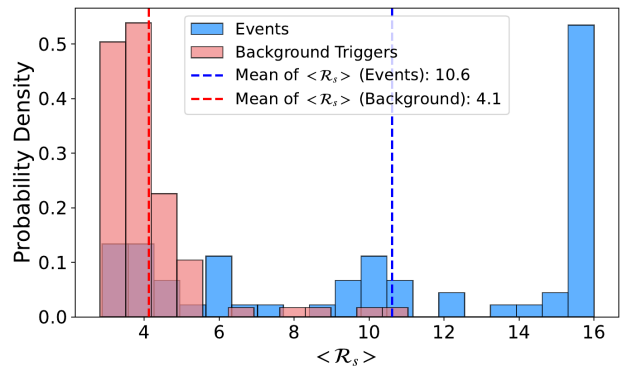


FIG. 6: Histograms of the ensemble-averaged ranking statistic $\langle \mathcal{R}_s \rangle$ for the foreground events (light blue) and background triggers (pink). The blue and red dashed vertical lines represent the mean value for each distribution, respectively.

Notice that the quasi-periodicity seen in Fig. 5 in the variations of \mathcal{R}_s for both candidate events and noise triggers, is probably associated with the morphology of a real signal or a glitch in the time-frequency space. This could be exploited for the classification of triggers (even in an online search) and is the subject of further investigation. This observation is relevant not only for AresGW, but also for other machine-learning codes that generate a ranking statistic in discrete time steps.

In the remainder of the text, we explicitly distinguish between \mathcal{R}_s and $\langle \mathcal{R}_s \rangle$.

D. Glitch removal with Gravity Spy

Gravity Spy [77–80] employs a convolutional neural network (CNN), a specialized deep learning algorithm designed for image recognition tasks, to classify glitches in LIGO detector data based on their time-frequency morphology. We utilized the dataset containing glitches detected by Gravity Spy in the O3a and O3b data, which can be found in [81], to minimize their influence on the background FAR calculated using AresGW. In practice, we excluded all triggers of the Omicron [82] dataset release for the O3a+O3b periods, since 97% of these triggers have been classified by Gravity Spy as belonging to one of the known glitch classes with ranking statistic > 0.5 . We utilized this approach both in creating a 10-year nearly glitch-free background, essential for determining the FAR, and in rejecting triggers detected by AresGW that turned out to be known glitches.

For trigger rejection, we focused on three main parameters: the start time and duration of the glitch, and the trigger time of AresGW. We examined whether a trigger was within a time interval equal to the duration of a known glitch ± 1 s, in which case it was removed from the data. The buffer of ± 1 s is set by the 1 s duration of the time segments examined by AresGW.

E. Parameter estimation

For the purpose of parameter estimation of new candidate gravitational wave signals, we used the Bayesian inference library for gravitational-wave astronomy, `Bilby` [83], with uniform distributions for priors. In particular, the priors for the detector-frame component masses m_1, m_2 correspond to a range of $[4M_\odot, 150M_\odot]$, and since we are sampling for chirp masses \mathcal{M} and mass ratios $q = m_2/m_1 \leq 1$, we set the component masses as constraints on the latter. In some cases, where the posterior distribution tails did not seem to drop to zero, we experimented with expanding the prior component mass range and/or the luminosity distance. The relation between redshift and luminosity distance is based on Planck15 cosmology [84].

Since multidimensionality is one of the main concerns when it comes to Bayesian inference applications in gravitational-wave astronomy, we chose `dynesty` [85] as a sampler. This method utilizes (Dynamic) Nested Sampling, combining the advantages of Markov Chain Monte Carlo (MCMC) algorithms, which concentrate on posterior estimation, with the ability of nested sampling to estimate evidences and sample from complex, multimodal distributions. This is achieved by adaptively allocating samples according to the posterior structure.

Each trigger was initially inspected using the IMRPhenomPv2 [86] waveform approximant, but our final results are produced with the IMRPhenomXPHM [76] model, which was also the waveform model for the injections on which AresGW was trained. Time and distance

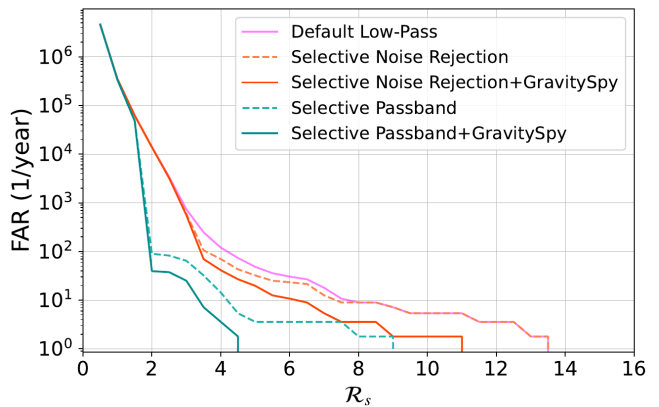


FIG. 7: False alarm rate (without time shifts) vs. ranking statistic for the 6.7-month O3 dataset. A reduction of FAR when applying our classification scheme and removal of known glitches, is observed.

Notice that the classification into Selective Noise Rejection and Selective Passband classes was only applied for $R_s > 3.5$ and $R_s > 2$, respectively (for smaller R_s , the lines are simply joined to the results of the Default Low-Pass class).

marginalization were also applied to each run (phase marginalization is formally invalid for precessing approximants). Finally, prior to conducting post-inference analysis on the candidate triggers, we verified the robustness of the obtained posterior distributions, by examining their resemblance to the Gaussian normal distribution (as assumed by Bilby’s Gaussian likelihood).

F. Consistency tests of candidate events

Each promising trigger we analyzed was subjected to several consistency tests, mainly utilizing routines from `PyCBC` [87]. One such test requires that the light-travel time between the two LIGO detectors is less than 10 ms, with an additional 5 ms window included to account for uncertainty in the estimated coalescence time at each detector, as discussed in [88]. A second important test is the waveform consistency test, which is based on the statistical veto χ^2 , and tests for non-Gaussianity of the residual, when a signal template is subtracted from the data. Specifically, we use the version presented in [89], with the number of bins chosen as

$$n = [0.4(f_{\text{peak}}/\text{Hz})^{2/3}]. \quad (3)$$

In Eq. (3), f_{peak} is the frequency observed at the point of maximum power output of the observed signal, corresponding to the time of merger [90]. These tests allow us to effectively reject a number of triggers that could be due to previously unidentified glitches.

Having performed the χ^2 test, we also used the *reweighted* SNR [87] as our main detection statistic.

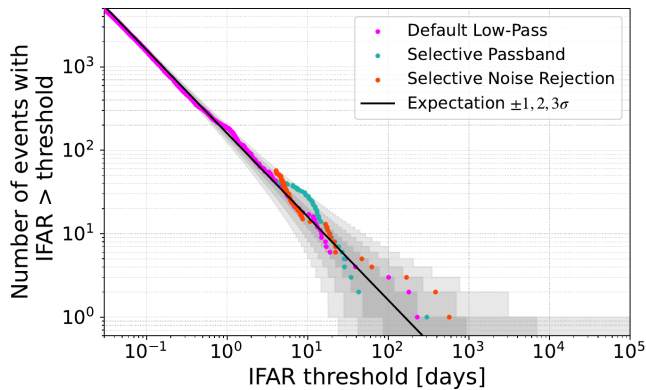


FIG. 8: Cumulative distribution of the inverse false alarm rate (without time shifts) of noise triggers using the O3 data. All three classes of our hierarchical classification yield distributions within 3σ of the expectation.

First, we calculate the SNR using matched filtering with the median reconstructed waveform, as obtained with parameter estimation using Bilby. This is done to identify any non-noise-like characteristics that may persist. If such features are found, it indicates that the model waveform h does not accurately match the non-Gaussian feature present in the data. Consequently, the SNR, ρ , is adjusted downwards. This can be expressed as [87]

$$\hat{\rho} = \rho \times \begin{cases} 1 & \text{if } \chi_r^2 \leq \nu, \\ \left[\frac{1}{2} + \frac{1}{2}(\chi_r^2/\nu)^3\right]^{-1/6} & \text{if } \chi_r^2 > \nu, \end{cases} \quad (4)$$

where $\nu = 2n - 2$ are the degrees of freedom. For real signals that have been accurately modeled, this is close to the true SNR, while for glitches it is much smaller, as a higher χ^2 down-weights it. For the network of the LIGO Livingston and LIGO Hanford detectors

$$\hat{\rho} = \sqrt{\hat{\rho}_L^2 + \hat{\rho}_H^2}, \quad (5)$$

is the reweighted network SNR, which we are going to evaluate for both known GW events and new candidate GW events.

III. BACKGROUND MODEL AND STATISTICS

A. False alarm rate from O3 data

After running AresGW on the entire 6.7-month data-quality dataset from the O3 observational period we then remove all known events previously published in the GWTC catalogs [4–7], the OGC catalogs [8–11] and the IAS catalogs [12–14], as well as the eight new events we identify here with $p_{\text{astro}} > 0.5$. From the remaining triggers (and after rescaling to a duration of one year) we obtain an estimate for the FAR distribution (without time

shifts) at a ranking statistic larger than \mathcal{R}_s , as shown in Fig. 7 (the initial ranking statistic was use here). Applying the Selective Noise Rejection filter, we find a small reduction in FAR. A larger reduction is obtained, when the Selective Passband filter is applied. Furthermore, the removal of known glitches using Gravity Spy is very effective in reducing the false alarm rate. Thus, with the Selective Passband filter, combined with glitch removal, a reduction between one and two orders of magnitude in FAR is obtained.

Fig. 8 shows the inverse FAR (IFAR) cumulative distribution [91] (without time shifts), when the previously published and new GW candidate events have been removed from the O3 data. For all three classes, the distribution of noise triggers is within 3σ of the expected distribution.

B. False alarm rate from time shifts

To better estimate the false alarm rate, we conducted an investigation on a time-shifted 10-year background dataset, from which known GW events, as well as glitches, identified in the Gravity Spy datasets, were removed (see Section IID). We also removed two additional obvious glitches of known class that were detected by AresGW, but were not included in the Gravity Spy database for O3. However, it is worth mentioning here, that despite removing those glitches, the dataset used for creating the background still contained some glitches. This fact, combined with the exclusive use of noise from O3a (even for O3b events), likely contributes to a somewhat higher (conservative) estimated FAR when using this method. The cumulative false alarm rate for all triggers with ranking statistic larger than a certain value \mathcal{R}_s will be denote as $\text{FAR}(> \mathcal{R}_s)$. This will be different for each of the three trigger classes introduced in Section IIB3. Fig. 9 shows a histogram of triggers generated with AresGW evaluating the 10-year background dataset, as a function of the ranking statistic \mathcal{R}_s and using a bin size of 0.053 (the initial ranking statistic was use here). All triggers shown in Fig. 9 were treated as Default Low-Pass and were *not* classified in one of the other two classes, as shown in Fig. 3.

Next, we applied our hierarchical classification scheme presented in Section IIB3 to all triggers above a certain ranking statistic threshold. More specifically, for the trigger classes Default Low-Pass and Selective Noise Rejection we used a threshold of $\mathcal{R}_s = 3.5$, whereas for the Selective Passband class we used a lower threshold of $\mathcal{R}_s = 2$ due to its significantly lower FAR.

Fig. 10 shows the cumulative false alarm rate for triggers classified as Default Low-Pass. Each dashed gray line represents 18 different realizations of a time-shifted background noise with a duration of 6.7 months. Adding all these different noise realizations to a single 10-year background, we obtain the cumulative FAR shown as the link line. With a lighter color, we also show the following

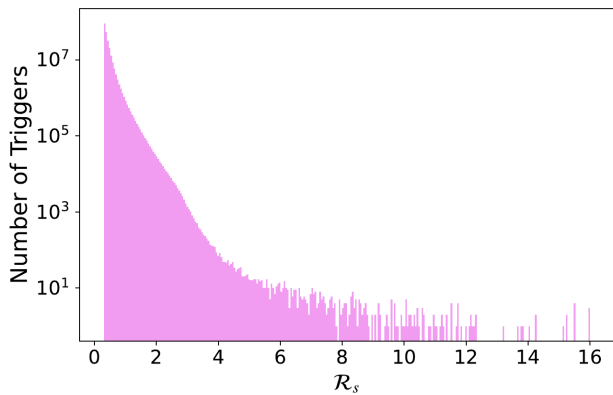


FIG. 9: Histogram of the Ranking Statistic for background noise over a 10-year period, based on time shifts of data-quality noise from O3a (see Sec. II A) without the glitches identified by Gravity Spy.

analytic fit

$$\begin{aligned} \log_{10}(\text{FAR}) = & -1.16 \times 10^{-4} \mathcal{R}_s^5 + 5.63 \times 10^{-3} \mathcal{R}_s^4 \\ & - 1.05 \times 10^{-1} \mathcal{R}_s^3 + 9.51 \times 10^{-1} \mathcal{R}_s^2 \quad (6) \\ & - 4.33 \mathcal{R}_s + 9.69. \end{aligned}$$

For $\mathcal{R}_s = 3.5$ the FAR is 280/year, whereas for $\mathcal{R}_s = 16$ the FAR drops to 0.34/year.

The darker pink line in Fig. 10 represents the outcome of AresGW applied to the actual O3 data when both LIGO detectors were observing (and with data-quality flag), with a real duration corresponding to approximately 6.7 months. Notice that the FAR for the actual O3 data is lower than any of the different 6.7 month noise realizations produced with time shifts of the 81-day O3a noise only. This could be explained, considering that the actual O3 noise encompasses both the O3a and O3b periods. In the latter period, the noise had significantly lower levels than in the former, due to some enhancements that were implemented to the LIGO detectors between O3a and O3b. A more suitable approach would involve splitting the analysis into two distinct periods: one for O3a and another for O3b, but due to time restrictions, we chose to use our O3a-based 10-year time-shifted background for producing a conservative FAR estimate also for triggers in the O3b period.

Similarly, Fig. 11 shows the cumulative false alarm rate for triggers classified as Selective Noise Rejection, including its analytic fit

$$\log_{10}(\text{FAR}) = -0.21 \mathcal{R}_s + 2.69. \quad (7)$$

For this class, the FAR is 90/year for $\mathcal{R}_s = 3.5$ and 0.22/year for $\mathcal{R}_s = 16$.

Finally, the cumulative false alarm rate for triggers classified as Selective Passband is shown in 12, including its analytic fit

$$\log_{10}(\text{FAR}) = -0.33 \mathcal{R}_s + 2.58. \quad (8)$$

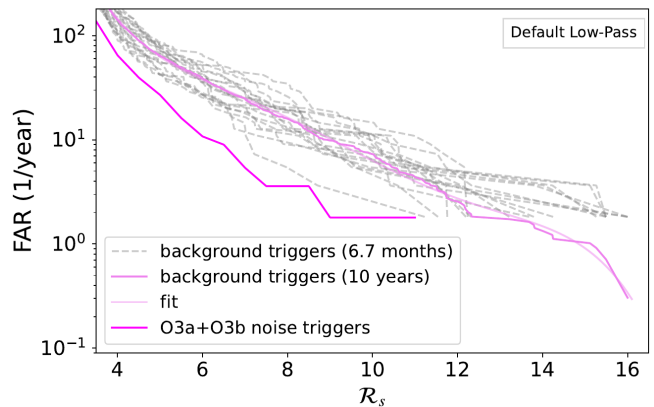


FIG. 10: False alarm rate vs. ranking statistic. Each dashed gray line represents a unique background noise period lasting 6.7 months. In contrast, the solid light-pink line represents the analytical relation of the False Alarm Rate (FAR) concerning the ranking statistic. The combination of these eighteen dashed grey instances results in the complete 10-year background, illustrated by the darker pink line, while the fuchsia line represents the outcome of AresGW applied to the authentic O3 data, with a duration corresponding to approximately 6.7 months for the two LIGO detectors.

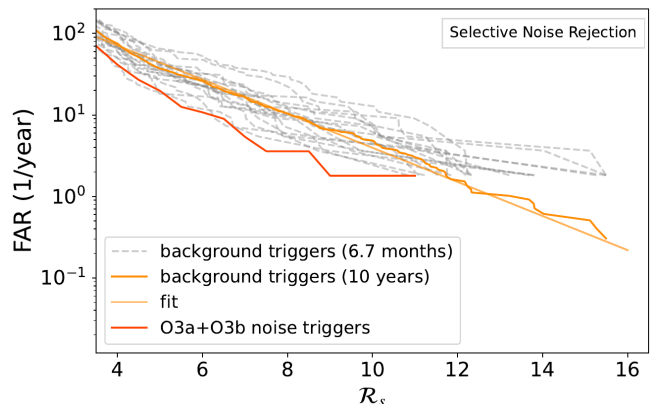


FIG. 11: Same as Fig. 10, but for the Selective Noise Rejection class of triggers.

At $\mathcal{R}_s = 3.5$, the FAR is 27/year, which motivated us to examine this class at even smaller ranking statistics values, reaching $\mathcal{R}_s = 2.0$, where the FAR was 84/year. On the other hand, at $\mathcal{R}_s = 16$ the FAR was just 0.0022/year, which means that this is the most sensitive class of triggers.

Investigating the gray lines in Figs. 10, 11 and 12, it is evident that the variance of false alarms as a function of \mathcal{R}_s for different noise realizations widens notably for the 6.7-month backgrounds as one examines higher values of \mathcal{R}_s . On the other hand, the cumulative FAR for the 10-year period shows a more consistent, almost straight-line dependence on \mathcal{R}_s , implying a smaller vari-

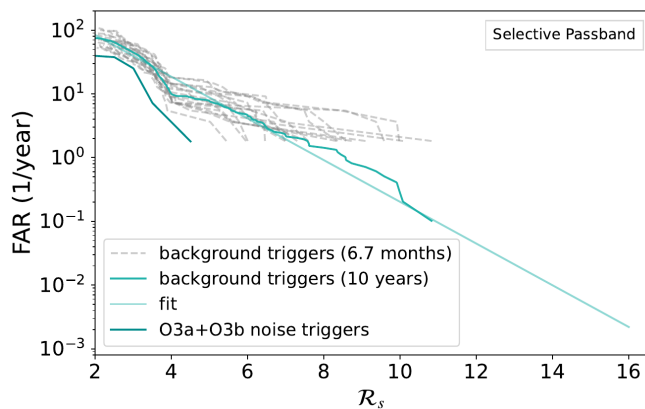


FIG. 12: Same as Fig. 10, but for the Selective Passband class.

ance. This phenomenon stems from the increased likelihood of additional noise interference, which can distort the outcomes. For example, consider a scenario where, over a span of 100 years, 10 false alarms are recorded at $\mathcal{R}_s = 10.0$. These occurrences may cluster within the initial ten years, or they might distribute evenly, one every ten years. In the former case, if the analysis were limited to those initial 10 years, false alarms at $\mathcal{R}_s = 10.0$ would appear as 1 per year, while the actual rate would be 0.1 per year. Therefore, longer-duration backgrounds yield more reliable results.

Notice that for the calculation of the false alarm rate in this subsection, the initial ranking statistic was used.

C. Background model

Consider a data set of N_b background events (either signals or background noise) that are ordered in terms of a ranking statistic x as $x_1 < x_2 < \dots < x_N$, where $x_1 = x_{\min}$ and $x_N = x_{\max}$. If we assume that the background events are samples from an inhomogeneous Poisson process and that θ are parameters that affect the shape of the distribution, then the differential rate for the background events can be defined as a function $b(x, \theta)$ as

$$\frac{dN_b}{dx} = b(x, \theta). \quad (9)$$

The cumulative rate of background events below a ranking statistic x is

$$B(x, \theta) \equiv \int_{x_{\min}}^x dx' b(x', \theta). \quad (10)$$

If R_b is the number of background events

$$R_b = B(x_{\max}, \theta), \quad (11)$$

we can normalize

$$\hat{B}(x, \theta) = B(x, \theta)/R_b. \quad (12)$$

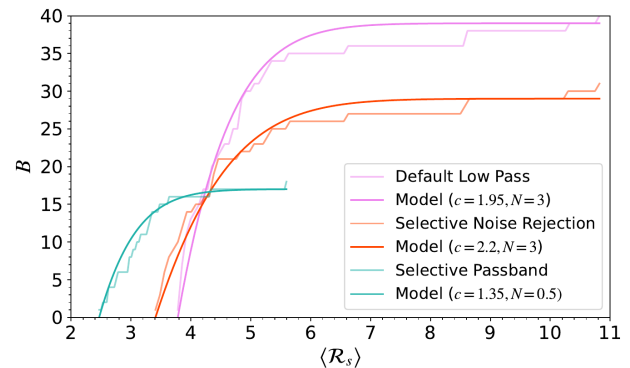


FIG. 13: Background distribution of the O3 data, for the different classes of our classification scheme. In all three cases, there is good agreement with our background model of Eq. (14).

For background triggers, the distribution can be modeled as

$$\hat{B}(x) = \left(\frac{1 + \operatorname{erf}\left(\frac{x}{\sqrt{2}}\right)}{2} \right)^N, \quad (13)$$

where N is a parameter, or

$$\hat{B}(x) = \frac{\left(1 + \operatorname{erf}\left(\frac{x}{\sqrt{2}}\right)\right)^N - \left(1 + \operatorname{erf}\left(\frac{x_{\min}}{\sqrt{2}}\right)\right)^N}{2^N - \left(1 + \operatorname{erf}\left(\frac{x_{\min}}{\sqrt{2}}\right)\right)^N}, \quad (14)$$

when the data are available above a threshold, $x > x_{\min}$ [92]. This expression was derived when the ranking statistic x is assumed to be the matched-filtering SNR. Since AresGW uses a different ranking statistic, we adopt the above expression as our background model, assuming $x = \mathcal{R}_s/c$, where we introduce the scaling parameter c . In addition, we found that assuming $R_b - 1$ or $R_b - 2$, instead of R_b yields better fits, as it offsets the larger variance at high \mathcal{R}_s .

In Fig. 13 we show the background distribution of the O3 data, for the different classes of our classification scheme. In all three cases, our background model of Eq. (14) fits the data well. We will use this analytics model for the background in the calculation of the astrophysical probability in Sec. V.

IV. FOREGROUND MODEL AND STATISTICS

A. Cumulative IFAR of all triggers

Similarly to Fig. 8, the cumulative IFAR distribution for all triggers (without removing known events) is shown in Fig. 14. For all three classes, the distribution is greater than 3σ of the expected noise distribution for IFAR = 1/d.

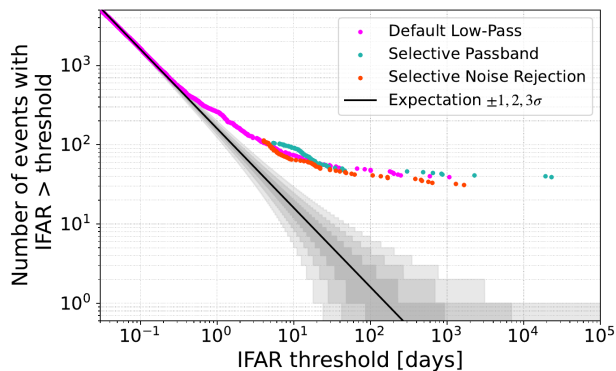


FIG. 14: Cumulative distribution of the inverse false alarm rate of all triggers (including known events) using the O3 data.

B. Foreground Model from Injections

If N_f are foreground events ordered in terms of a ranking statistic x as $x_1 < x_2 < \dots < x_N$, where $x_1 = x_{\min}$ and $x_N = x_{\max}$, then the differential rate for the foreground events can be defined as a function $f(x, \theta)$ as [92]

$$\frac{dN_f}{dx} = f(x, \theta). \quad (15)$$

The cumulative rate of foreground events below a ranking statistic x is

$$F(x, \theta) \equiv \int_{x_{\min}}^x dx' f(x', \theta). \quad (16)$$

If R_f is the total number of foreground events

$$R_f = F(x_{\max}, \theta), \quad (17)$$

we can normalize

$$\hat{F}(x, \theta) = F(x, \theta)/R_f. \quad (18)$$

Since our ranking statistic does not coincide with the SNR used in other foreground models (see [92]), we determined the foreground model $\hat{F}(x, \theta)$ using the LVK O3 injections [93] in the 80-day O3a noise created for the MLGWSC-1 challenge [72].

The left panel of Fig. 15 shows the un-normalized data $F(\mathcal{R}_s)$ for the three classes of our classification scheme, as obtained by analyzing the injections with AresGW. We find that the data is in excellent agreement with the model

$$F(x) = a(x - x_{\min})^b, \quad (19)$$

where $x = \mathcal{R}_s$ (for the injections we used the initial ranking statistic of each trigger). The exponent b is obtained as $b = 0.616$ for the Default Low-Pass class, $b = 0.802$ for the Selective Noise Rejection class, and $b = 0.830$ for the Selective Passband class.

The right panel of Fig. 15 shows the corresponding un-normalized data $F(\langle \mathcal{R}_s \rangle)$ for the three classes of our classification scheme, as obtained by analyzing the known O3 events with AresGW (notice that a significant fraction of known events accumulate at the highest ranking statistic $\langle \mathcal{R}_s \rangle = 16$ and are not included in the model). For the O3 events, we used the mean ranking statistic, as discussed in Sec. II C. In each panel, we also show the agreement of the foreground model of Eq. (19) with the O3 data, when using the same value for the exponent b , as obtained with injections in the left panel of Fig. 15. The agreement is very satisfactory, and hence we adopt Eq. (19) as our foreground model for the O3 events, using their ensemble-averaged $\langle \mathcal{R}_s \rangle$ and with the exponent b determined by injections.

V. ASTROPHYSICAL PROBABILITY

Inverting Eqs. (10) and (16), we obtain the differential rates

$$b(\langle \mathcal{R}_s \rangle) = \frac{dB}{d\langle \mathcal{R}_s \rangle}, \quad (20)$$

and

$$f(\langle \mathcal{R}_s \rangle) = \frac{dF}{d\langle \mathcal{R}_s \rangle}. \quad (21)$$

The astrophysical probability of a candidate event is then [91, 92, 94]

$$p_{\text{astro}} = \frac{f(\langle \mathcal{R}_s \rangle)}{b(\langle \mathcal{R}_s \rangle) + f(\langle \mathcal{R}_s \rangle)}. \quad (22)$$

Since AresGW has been trained in a specific mass range, we treat this range as a single band. In the future, we aim at combining different versions of AresGW, each trained in a different segment of partially overlapping bands and use a multi-band expression for defining the astrophysical probability, as in [91].

In Fig. 16 we show p_{astro} as a function of the (ensemble-averaged) ranking statistic $\langle \mathcal{R}_s \rangle$ for the three classes of our classification scheme. Candidate events have $p_{\text{astro}} > 0.5$ for $\langle \mathcal{R}_s \rangle = 5.79$ (Default Low-Pass), $\langle \mathcal{R}_s \rangle = 6.0$ (Selective Noise Rejection), and $\langle \mathcal{R}_s \rangle = 3.91$ (Selective Passband).

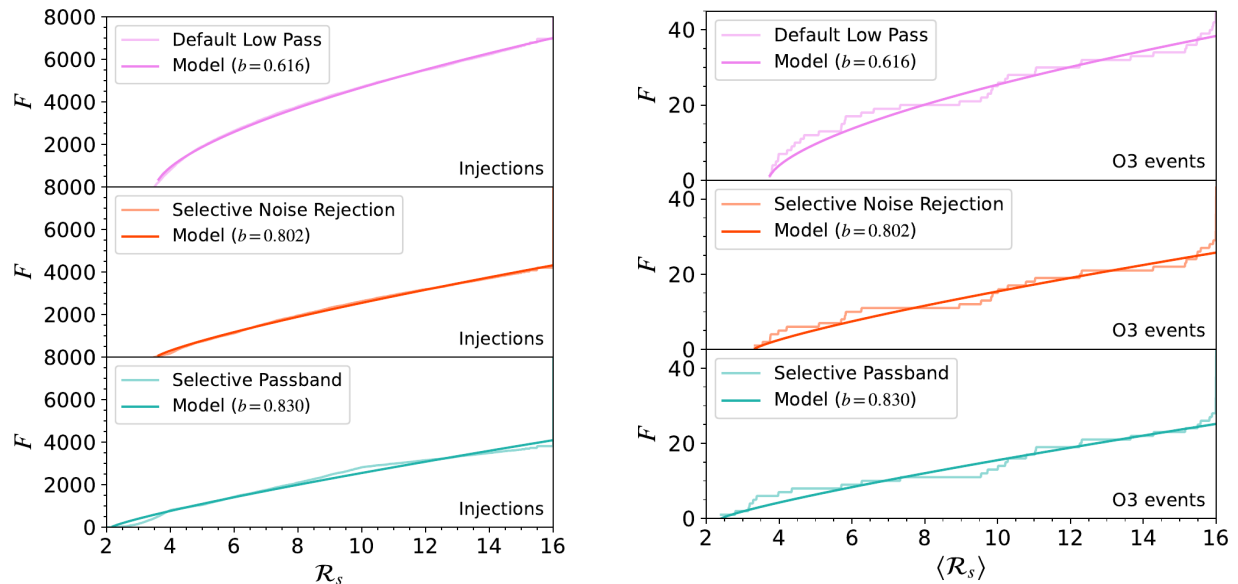


FIG. 15: *Left panel:* Cumulative rate F of foreground events for injections in O3a noise. There is excellent agreement with the foreground model Eq. (19). *Right panel:* Cumulative rate F of known foreground O3 events. There is very good agreement with the foreground model Eq. (19), when the same exponent b is used as obtained from the injections.

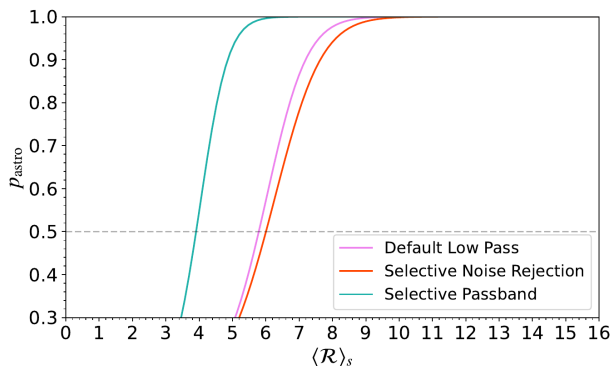


FIG. 16: The astrophysical probability p_{astro} as a function of the (ensemble-averaged) ranking statistic $\langle \mathcal{R}_s \rangle$ for the three classes of our classification scheme.

VI. CONFIRMATION OF KNOWN GW EVENTS IN O3 DATA

In this section, we will examine the performance of AresGW on gravitational-wave events that were previously identified and compare it to algorithms used in the published GWTC [4–7], OGC [8–11], and IAS [12–14] catalogs. It is essential to note that AresGW utilizes two channels; it is trained on data from the two LIGO detectors, when both were active (Virgo data are not used in

the training)². Therefore, our main analyses pertain to BBH events detected when both the Livingston and Hanford detectors were operational. Nevertheless, we show in Sec. VID that AresGW generalizes well to events that were detected by one of the LIGO detectors, with Virgo as the second detector, even though it has not been trained on Virgo data.

The Gravitational-wave Transient Catalog (GWTC) [4–7] represents a comprehensive compendium of gravitational wave events, published by the the LIGO/Virgo/KAGRA collaboration. Here, we will consider those GWTC events that have been characterized as confident detections. These detections are deemed to have a probability greater than 0.5 of being a gravitational wave signal rather than instrumental noise, assuming a compact binary coalescence source, as determined by at least one of the associated search pipelines. The algorithms contributing to these catalogs encompass `cwb`, `gstlal`, `mbta`, `pycbc_bbh`, and `pycbc_broad`, which employ matched filtering using specific waveform models or wavelet techniques for unmodeled burst detection. Proceeding to the four OGC catalogs [8–11], they confirm known GWTC events and report additional candidate events, using a matched filtering technique as well. Meanwhile, in recent searches, the IAS algorithm [12–14]

² If one or both LIGO detectors were inactive during a specific time frame, the network does not generate a trigger for that period.

specifically targeted signals that could originate from the lower or upper mass gap, but also reported new candidate events that fall within our effective training range, using different versions of their matched-filtering detection algorithm.

A. Known events within our effective training range

Considering all three event catalogs, GWTC, OGC, and IAS, along with their respective sublists, there is a total of 43 gravitational wave events within our designated training range. It is crucial to reiterate that although our training dataset comprises events with source masses falling within the range ($7M_{\odot}, 50M_{\odot}$), we evaluate events within our effective training range, which has the additional restriction of \mathcal{M} being in the range ($10M_{\odot}, 40M_{\odot}$). In this range, there are 36 known GWTC events, another 4 that were first reported by OGC and 3 additional reported by IAS (a total of 43 different known events).

With AresGW, we confidently detect 34 of the 43 known detections in its effective training range, with astrophysical probability $p_{\text{astro}} > 0.5$. Out of the 9 candidate events that AresGW reports with $p_{\text{astro}} < 0.5$, 4 were previously reported with astrophysical probabilities only slightly greater than 0.5: 1 in the GWTC, 2 in the IAS, and 1 in the OGC catalogs, with p_{astro} values of 0.54, 0.63, 0.56, and 0.5, respectively.

Of the 34 known events that we confirm with AresGW, we obtain 30 events with $p_{\text{astro}} = 1.0$. Furthermore, we find 28 events with $\text{FAR} < 1/\text{y}$. In Table I we list the published p_{astro} , FAR and source parameters m_1, m_2, \mathcal{M} for the 43 known events. In addition, we report the p_{astro} , FAR, and ranking statistic $\langle \mathcal{R}_s \rangle$, as obtained with AresGW. We find 33 out of 34 events that we confirm, to have p_{astro} higher than or equal to their published value.

In Section VIC, we present a more detailed comparison between AresGW and the individual pipelines involved in the GWTC/OGC/IAS catalogs.

B. Known events outside our effective training range

The GWTC/OGC/IAS catalogs contain 55 events that fall outside of our effective training range (the majority of these were reported in the IAS catalog). Even though AresGW was trained mainly on data that fall within our effective training range, so that it has not seen samples for most of these 55 events, we find that it was still able to detect 10 of them with $p_{\text{astro}} \geq 0.99$ (see Table II).

The observation that our algorithm recognizes one-fifth of all events outside its effective training range underscores the robustness of our deep learning detection code in identifying gravitational wave signals. It also implies that with additional training in other mass regions,

AresGW should be able to detect events with the same efficiency as in the current ($10M_{\odot} < \mathcal{M} < 40M_{\odot}$) range.

To further emphasize the network's effectiveness beyond its familiar waveform region, we highlight its detection of a signal like GW191109.010717. This event features source masses of $65.0 M_{\odot}$ and $47.0M_{\odot}$, and \mathcal{M} of $47.50M_{\odot}$, parameters considerably larger than those in the effective training dataset. AresGW also detected several other signals with at least one parameter significantly different from those in the effective training dataset. Notable examples include GW190519.153544, GW190706.222641, GW191109.010717 and GW190711.030756. In fact, the first three of these events were detected with the maximum $\langle \mathcal{R}_s \rangle$ value allowed by double machine precision ($\langle \mathcal{R}_s \rangle = 16$).

C. Comparison of sensitivity between AresGW and other search pipelines

Commencing with the individual algorithms that contribute to the GWTC catalog, among the 43 published events within our effective training range, the `mbta` algorithm detects 27, `pycbc_bbh` 31, `pycbc_broad` 20, `gstlal` 27, and `cwb` 7 events, respectively. Note that several events are reported by multiple pipelines. The number of different events reported by all GWTC pipelines within our effective training range is 36. On the other hand, our enhanced version of AresGW detects 34 events in the same range.

The algorithm used in the OGC catalog detected 37 events in this range. For events reported in the IAS publications, we distinguish between those reported in [12, 13], which we designate as IAS_a and those in [14], which we designate as IAS_b . IAS_a detected 34 events in this range, whereas IAS_b detected 36 events in this range.

In Section VII we present 8 new candidate events, detected by AresGW. This brings the total number of events detected by AresGW within its effective training range to 42, exceeding the total number of events detected by other pipelines.

Table III summarizes the above comparisons of the number of distinct BBH events within our effective training range that are reported with $p_{\text{astro}} > 0.5$ by the different detection pipelines.

Furthermore, considering different events in this range, it is interesting to compare the detections that have been reported with $p_{\text{astro}} = 1.0$ by the different pipelines. With this requirement, the GWTC algorithms detected 21 events and AresGW detected 30 (without including new events). The algorithm used in the OGC catalog detected 24 events, and the IAS_a and IAS_b algorithms detected 20 and 18, respectively. In [15], 21 events with $p_{\text{astro}} = 1.0$ were reported with the `pycbc_KDE` algorithm. Table IV summarizes the above comparison.

In short, AresGW shows exceptional sensitivity in the detection of gravitational waves, within its effective train-

TABLE I: AresGW Performance on all previously detected events in the dataset.

#	Event Name	Catalog	p_{astro} (AresGW)	p_{astro}^a	FAR (1/yr) (AresGW)	FAR (1/yr) ^{b c}	$\langle \mathcal{R}_s \rangle$ (AresGW)	\mathcal{M} (M_\odot)	m_1 (M_\odot)	m_2 (M_\odot)	Class
1	GW190408_181802	GWTC	1.00	1.00	≤ 0.0020	≤ 0.00001	≥ 16.0	18.5	24.8	18.5	Selective Passband
2	GW190412_053044	GWTC	1.00	1.00	≤ 0.0020	≤ 0.00001	≥ 16.0	13.3	27.7	9.0	Selective Passband
3	GW190421_213856	GWTC	1.00	1.00	≤ 0.0020	0.0028	≥ 16.0	31.4	42.0	32.0	Selective Passband
4	GW190513_205428	GWTC	1.00	1.00	≤ 0.0020	0.000013	≥ 16.0	21.8	36.0	18.3	Selective Passband
5	GW190727_060333	GWTC	1.00	1.00	≤ 0.0020	≤ 0.00001	≥ 16.0	29.4	38.9	30.2	Selective Passband
6	GW190803_022701	GWTC	1.00	0.97	≤ 0.0020	0.39	≥ 16.0	27.6	37.7	27.6	Selective Passband
7	GW190828_063405	GWTC	1.00	1.00	≤ 0.0020	≤ 0.00001	≥ 16.0	24.6	31.9	25.8	Selective Passband
8	GW190915_235702	GWTC	1.00	1.00	≤ 0.0020	≤ 0.00001	≥ 16.0	24.4	32.6	24.5	Selective Passband
9	GW191215_223052	GWTC	1.00	≥ 0.99	≤ 0.0020	≤ 0.00001	≥ 16.0	18.4	24.9	18.1	Selective Passband
10	GW191222_033537	GWTC	1.00	≥ 0.99	≤ 0.0020	≤ 0.00001	≥ 16.0	33.8	45.1	34.7	Selective Passband
11	GW200128_022011	GWTC	1.00	≥ 0.99	≤ 0.0020	0.0043	≥ 16.0	32.0	42.2	32.6	Selective Passband
12	GW200129_065458	GWTC	1.00	≥ 0.99	≤ 0.0020	≤ 0.00001	≥ 16.0	27.2	34.5	29.0	Selective Passband
13	GW200208_130117	GWTC	1.00	≥ 0.99	≤ 0.0020	0.00031	≥ 16.0	27.7	37.7	27.4	Selective Passband
14	GW200209_085452	GWTC	1.00	0.97	≤ 0.0020	12	≥ 16.0	26.7	35.6	27.1	Selective Passband
15	GW200219_094415	GWTC	1.00	≥ 0.99	≤ 0.0020	0.00099	≥ 16.0	27.6	37.5	27.9	Selective Passband
16	GW200224_222234	GWTC	1.00	≥ 0.99	≤ 0.0020	≤ 0.00001	≥ 16.0	31.1	40.0	32.7	Selective Passband
17	GW200311_115853	GWTC	1.00	≥ 0.99	≤ 0.0020	≤ 0.00001	≥ 16.0	26.6	34.2	27.7	Selective Passband
18	GW190916_200658	OGC	1.00	0.90	0.0022	4.55	15.9	27.9	43.9	24.8	Selective Passband
19	GW190719_215514	GWTC	1.00	0.92	0.0023	0.63	15.8	22.8	36.6	19.9	Selective Passband
20	GW190512_180714	GWTC	1.00	1.00	0.0029	≤ 0.00001	15.5	14.6	23.2	12.5	Selective Passband
21	GW190731_140936	GWTC	1.00	0.83	0.0037	1.9	15.2	29.7	41.8	29.0	Selective Passband
22	GW190527_092055	GWTC	1.00	0.85	0.0073	0.23	14.3	23.9	35.6	22.2	Selective Passband
23	GW190521_074359	GWTC	1.00	1.00	0.01	≤ 0.00001	13.7	32.8	43.4	33.4	Selective Passband
24	GW190413_052954	GWTC	1.00	0.93	0.033	0.82	12.3	24.5	33.7	24.2	Selective Passband
25	GW190517_055101	GWTC	1.00	1.00	0.033	0.00035	12.3	26.5	39.2	24.0	Selective Passband
26	GW190503_185404	GWTC	1.00	1.00	0.089	≤ 0.00001	11.0	29.3	41.3	28.3	Selective Passband
27	GW200305_084739	OGC	1.00	0.59	0.1	50	10.8	24.0	33.8	27.5	Selective Passband
28	GW191230_180458	GWTC	1.00	0.96	0.16	0.42	10.2	36.5	49.4	37.0	Selective Passband
29	GW191204_110529	GWTC	1.00	0.74	1.5	3.3	7.3	19.8	27.3	19.2	Selective Passband
30	GW200225_060421	GWTC	1.00	≥ 0.99	4.3	≤ 0.000011	9.8	14.2	19.3	14.0	Selective Noise Rejection
31	GW190906_054335	IAS	0.99	0.61	0.22	1.4	15.9	21.90	37.00	24.00	Selective Noise Rejection
32	GW200220_124850	GWTC	0.99	0.83	4.1	1800	9.9	28.2	38.9	27.9	Selective Noise Rejection
33	GW200106_134123	OGC	0.95	0.69	7.9	17	5.1	29.7	44.0	27.4	Selective Passband
34	GW200322_091133	GWTC	0.55	0.62	18.2	450	4.0	15.0	38.0	11.3	Selective Passband
35	GW190926_050336	OGC	0.42	0.92	31	3.7	5.7	26.2	40.0	23.8	Selective Noise Rejection
36	GW190828_065509	GWTC	0.22	1.00	91	0.000035	4.6	13.4	23.7	10.4	Default Low-Pass
37	GW190514_065416	GWTC	0.16	0.76	64	2.8	4.2	29.1	40.9	28.4	Selective Noise Rejection
38	GW190805_211137	GWTC	0.15	0.95	71	0.63	4.0	31.9	46.2	30.6	Selective Noise Rejection
39	GW200306_093714	GWTC	0.14	0.81	78	410	3.8	17.5	28.3	14.8	Selective Noise Rejection
40	GW200318_191337	OGC	0.0	0.97	582	2.0	3.1	33.5	49.1	31.6	Default Low-Pass
41	GW190530_030659	IAS	0.0	0.63	1815	0.63	2.6	21.90	36.0	18.0	Default Low-Pass
42	GW190404_142514	OGC	0.0	0.50	4309	50	2.3	13.8	21.6	12.1	Default Low-Pass
43	GW200301_211019	IAS	0.0	0.56	80380	0.4	2.1	14.74	22.0	13.2	Default Low-Pass

^a For GWTC, the p_{astro} given is the best one provided among all its algorithms.

^b IAS FAR is computed within bank.

^c GTWC FAR is the one corresponding to the algorithm that provided the best p_{astro} .

ing range. It detects a larger number of events compared to other algorithms that are based on matched filtering or unmodeled search. A key factor for this is the fact that AresGW is simultaneously trained on injections in real O3a noise for both detectors, reporting a single ranking statistic for a pair of detectors. In contrast, other pipelines may reject candidate events if they don't pass

an SNR threshold in individual detectors.

D. Generalization to Virgo data

In Sections II A and VI we discussed AresGW's performance on O3 data when considering events that were

TABLE II: AresGW Performance on events out of the dataset.

#	Event Name	Catalog	p_{astro} (AresGW)	p_{astro}	FAR (1/yr) (AresGW)	FAR (1/yr)	$\langle \mathcal{R}_s \rangle$ (AresGW)	\mathcal{M} (M_{\odot})	m_1 (M_{\odot})	m_2 (M_{\odot})	Class
1	GW191127.050227	GWTC	1.00	0.74	≤ 0.0020	4.1	≥ 16.0	29.90	53.0	24.0	Selective Passband
2	GW190413.134308	GWTC	1.00	0.99	0.0027	0.18	15.6	33.30	51.3	30.4	Selective Passband
3	GW191204.171526	GWTC	1.00	≥ 0.99	0.0029	≤ 0.00001	15.5	8.56	11.7	8.4	Selective Passband
4	GW190706.222641	GWTC	1.00	1.00	0.083	0.00005	11.1	45.60	74.0	39.4	Selective Passband
5	GW190519.153544	GWTC	1.00	1.00	0.15	≤ 0.00001	10.3	44.30	65.1	40.8	Selective Passband
6	GW191109.010717	GWTC	1.00	≥ 0.99	0.24	0.00018	9.7	47.50	65.0	47.0	Selective Passband
7	GW190701.203306	GWTC	1.00	1.00	0.32	0.56	15.2	40.20	54.1	40.5	Selective Noise Rejection
8	GW190707.093326	GWTC	1.00	1.00	3.2	≤ 0.00001	6.3	8.40	12.1	7.9	Selective Passband
9	GW190728.064510	GWTC	1.00	1.00	3.9	≤ 0.00001	10.0	8.6	12.5	8.0	Selective Noise Rejection
10	GW190711.030756	IAS	0.99	1.00	5.5	0.02584	9.3	29.8	71.7	17.9	Selective Noise Rejection

TABLE III: Performance of AresGW in comparison to the GWTC, OGC, IAS and pycbc_KDE [15] algorithms on all 51 candidate events (43 previously published plus 8 new events detected by AresGW) that are within the effective training range.

cwb	pycbc_broad	mbta	gstlal	pycbc_KDE	pycbc_bbh	IAS_a	IAS_b	OGC	AresGW
7	20	27	27	29	31	34	36	37	42

detected by the two LIGO detectors (without taking into account Virgo data, when they were available). To further assess the generalizability of our detection code, we extended our analysis to data from the Virgo detector, when combined with one of the two LIGO detectors. In essence, we evaluated published BBH merger events that were detected by either the LIGO Hanford and Virgo network or the LIGO Livingston and Virgo network of detectors (when the third detector was not operating). In the GWTC catalogs there are 8 such events during the O3 period, see Table V (this number does not include detections, when all three detectors were observing). Although we did not estimate a false alarm rate for these events, it is encouraging that half of them were detected with a $\langle \mathcal{R}_s \rangle \geq 5.6$.

This highlights the impressive ability of AresGW to generalize. Its performance on previously unseen, noisier compared to the LIGO detectors, data from the Virgo detector, suggests the potential for deployment in future observing runs without necessitating retraining. Furthermore, there is promise for uncovering new gravitational wave events by adapting the code using specifically Virgo detector data alongside that of another detector through direct analysis of noise from another observing period. Moreover, in the future, the use of a three-channel AresGW pipeline seems to hold great potential in achieving higher detection sensitivities, as the code will be trained on simultaneous injections for three different detectors and will evaluate the three-detector data as a single, concatenated data segment, producing a single ranking statistic.

E. Generalization to O1 and O2 data

Upon observing AresGW’s ability to adjust to Virgo’s noise, we aimed to further assess the generalization capacity of our code by evaluating it on the data of the O1 and O2 observation periods [75]. As shown in Table VI, our machine learning code validated 5 of the 6 events that were previously detected during O2 with a maximum ranking statistic value $\langle \mathcal{R}_s \rangle$ of 16.0, while it, also, detected the sixth event with $\mathcal{R}_s = 15.4$. Moreover, it identified the first gravitational wave event ever detected in the O1 period (GW150914) with the maximum ranking statistic value of $\langle \mathcal{R}_s \rangle = 16$. Therefore, AresGW detected all events (but one) within its training range in the O1 and O2 periods, with a $\langle \mathcal{R}_s \rangle \geq 15.4$. The only exception was the O1 event GW151012, which was detected with a lower ranking statistic³.

The above findings, alongside our neural network’s capacity to generalize effectively to Virgo’s data, highlight AresGW’s impressive capability for generalization. This aspect inspires confidence in the possibility of detecting, with further analysis, new gravitational waves using O1 and O2 data too, all without necessarily retraining the network. Furthermore, it holds the same promise for the O4 observing run, in which the noise levels for the two LIGO detectors have decreased significantly.

³ The other O1 event, GW151226, was assigned a very low ranking statistic by AresGW, but it’s outside its nominal effective training range.

TABLE IV: Performance of AresGW in comparison to the GWTC, OGC, IAS and pycbc_KDE [15] algorithms on all *previously published* events that were reported with $p_{\text{astro}} = 1$ and are within the effective training range of AresGW (this does not include the new AresGW candidate events).

GWTC	pycbc_KDE	IAS.a	IAS.b	OGC	AresGW
21	21	20	18	24	30

TABLE V: AresGW Performance on BBH events detected while only one of the LIGO detectors and the Virgo detector were active (this list does not include detections, when all three detectors were observing).

#	Event Name	Catalog	Detectors	$\langle \mathcal{R}_s \rangle$	\mathcal{M} (M_{\odot})	m_1 (M_{\odot})	m_2 (M_{\odot})
1	GW191216_213338	GWTC	HV	11.5	8.33	12.1	7.7
2	GW190630_185205	GWTC	LV	8.2	25.1	35.1	24.0
3	GW200112_155838	GWTC	LV	7.2	27.4	35.6	28.3
4	GW190708_232457	GWTC	LV	5.6	13.1	19.8	11.6
5	GW190620_030421	GWTC	LV	3.2	38.1	58.0	35.0
6	GW200302_015811	GWTC	HV	2.5	23.4	37.8	20.0
7	GW190925_232845	GWTC	HV	2.3	15.6	20.8	15.5
8	GW190910_112807	GWTC	LV	1.4	33.5	43.8	34.2

TABLE VI: AresGW Performance on BBH events detected on O1 and O2 from both LIGO detectors.

#	Event Name	Catalog	$\langle \mathcal{R}_s \rangle$	\mathcal{M} (M_{\odot})	m_1 (M_{\odot})	m_2 (M_{\odot})
1	GW170104	GWTC	≥ 16.0	21.1	28.7	20.8
2	GW170729	GWTC	≥ 16.0	34.6	54.7	30.2
3	GW170809	GWTC	≥ 16.0	24.8	34.1	24.2
4	GW170814	GWTC	≥ 16.0	24.1	30.9	24.9
5	GW170823	GWTC	≥ 16.0	28.6	38.3	29.0
6	GW150914	GWTC	≥ 16.0	27.9	34.6	30.0
7	GW170818	GWTC	15.4	26.8	34.8	27.6
8	GW151012	GWTC	2.5	15.6	24.8	13.6
9	GW151226	GWTC	1.3	8.9	14.2	7.5

VII. NEW ARESGW CANDIDATE EVENTS

In addition to confirming previously published events, we have obtained 8 new triggers with $p_{\text{astro}} \geq 0.5$. We stress that only one of these new triggers, GW190607_093827, is included in the Deep Extended Catalog of GWTC-2.1, which comprises 1201 subthreshold triggers with a FAR less than 2 per day [6]. Here, we present several tests to establish the astrophysical relevance of these new candidate events. We also perform parameter estimation and discuss their population properties.

A. False alarm rate and consistency tests

Among all triggers with a ranking statistic $\langle \mathcal{R}_s \rangle$ exceeding 3.5 (or 2.0 for the Selective Passband class) we focused only on those exhibiting visible features consistent with the expected chirp produced by BBH mergers

in time-frequency spectrograms. These triggers were further investigated, including time and consistency assessments. From this analysis, we present the triggers that have successfully passed all relevant tests, thus identifying them as new candidate events.

In Table VII we present several properties of each new candidate signal, such as their GPS timestamp, ranking statistic $\langle \mathcal{R}_s \rangle$, false alarm rate FAR and astrophysical probability p_{astro} , as well as the trigger class, according to the hierarchical classification we introduced in Section II B 3. Furthermore, after performing the parameter estimation for each candidate signal (see Section VII B) we obtained the time delay of each signal between the two LIGO detectors and the χ^2 for the signal at the two detectors, χ_L^2 and χ_H^2 , which we also list in Table VII. We note that all 8 of our new candidate events successfully pass those necessary consistency tests that were also used in previously published catalogs of GW events.

In Fig.17 we present our estimate of the cumulative FAR($> \mathcal{R}_s$) as a function of the ranking statistic for the new candidate events. The estimates are based on the analytical fits for each trigger class, see Eqs.(6), (7) and (8) in Section III B. Evidently, the Selective Noise Rejection triggers exhibit a lower FAR for equivalent ranking statistic values compared to the Default Low-Pass triggers. Furthermore, the Selective Passband triggers demonstrate a significant reduction in the FAR across several orders of magnitude, compared to both the Selective Noise Rejection and the Default Low-Pass triggers. This observation underscores the superiority of the Selective Passband trigger class, in terms of a lower FAR estimate.

Had we kept all triggers above $\langle \mathcal{R}_s \rangle$ as Default Low-Pass and without removing known glitches, this would amount to $O(150)$ triggers for further examination. Through the application of the classification sys-

TABLE VII: New candidate events identified by AresGW.

#	Event Name	GPS Time (s)	p_{astro}	FAR (1/yr)	$\langle \mathcal{R}_s \rangle$	Time delay (s)	χ_L^2	χ_H^2	Class
1	GW190511_125545	1241614563.77	1.00	0.27	9.54	0.0027	1.16	1.46	Selective Passband
2	GW190614_134749	1244555287.93	0.99	4.6	5.80	0.0012	0.65	0.80	Selective Passband
3	GW190607_083827	1243931925.99	0.99	6.5	8.95	0.0056	0.90	0.48	Selective Noise Rejection
4	GW190904_104631	1251629209.01	0.72	14	4.35	0.0002	0.38	0.71	Selective Passband
5	GW190523_085933	1242637191.44	0.68	20	6.60	0.0054	0.75	1.39	Selective Noise Rejection
6	GW200208_211609	1265231787.68	0.55	18	4.0	0.0063	0.69	0.98	Selective Passband
7	GW190705_164632	1246380410.88	0.51	49	5.82	0.0103	1.05	0.98	Default Low-Pass*
8	GW190426_082124	1240302101.93	0.50	20	3.91	0.0007	1.48	0.53	Selective Passband

* This event also classified as Selective Noise Rejection, but it has the best p_{astro} as Default Low-Pass.

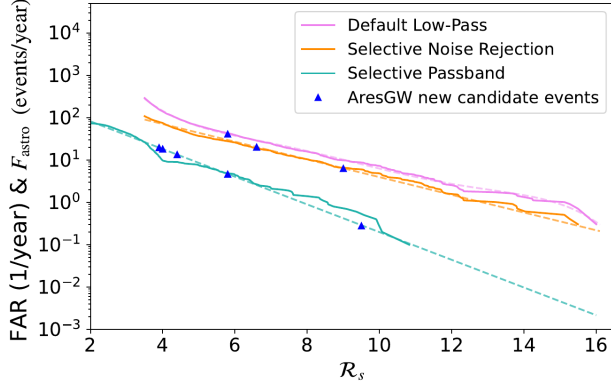


FIG. 17: False alarm rate based on 10-year time shifts and corresponding analytic fits (dashed lines) for the three classes of triggers. The new events identified by AresGW are also shown.

tem alongside the glitch removal process though, we observed 22 noise triggers in the Selective Passband class and 39 in the Selective Noise Rejection class⁴, therefore, we constructed wavelet-based Qp-transform spectrograms [95, 96] for those triggers. The Qp-transform spectrograms were then visually inspected, and a few obvious glitches, which were not caught by Gravity Spy, were also eliminated.

Specifically for the Selective Passband triggers, we followed the exact same procedure described above, but starting from a ranking statistic threshold of $\langle \mathcal{R}_s \rangle$. Between the ranking statistic values of 2.0 and 3.5, approximately 40 additional triggers were included for inspection. Subsequently, we identified a number of $O(10)$ promising gravitational wave candidate events for further inspection.

Fig. 18 shows the astrophysical probability vs. the false alarm rate, as obtained with AresGW, for both previously published and new candidate events identified.

⁴ Following glitch removal, the Default Low-Pass class exhibited 76 noise triggers.

The p_{astro} and FAR values obtained with AresGW are within the total spread of values of previously published events in the GWTC/OGC/IAS catalogs.

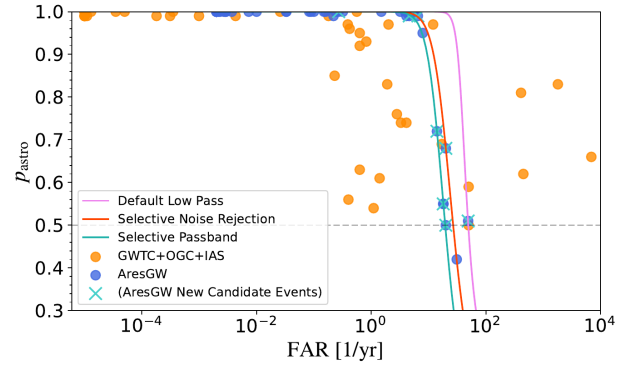


FIG. 18: Astrophysical probability vs. false alarm rate for candidate events identified with AresGW. Both previously published and new events are shown. For comparison, the p_{astro} vs. FAR values of previously published events in the GWTC/OGC/IAS catalogs are shown.

Fig. 19 shows the Qp-transform spectrograms for the 8 new GW candidate events identified by AresGW. The familiar shape of a chirping signal is prominent in these spectrograms.

B. Parameter estimation

We performed parameter estimation for all of our new candidate events, using Bilby [83] (see Section II E) and assuming the IMRPhenomXPHM waveform model, which has the component black hole masses $m_{1,2}$, their respective dimensionless spin magnitudes $s_{1,2}$, the tilt angle between their spins and the orbital angular momentum $\theta_{1,2}$, and the two spin vectors describing the azimuthal angle separating the spin vectors $\delta\phi$ and the cone of precession about the system's angular momentum as the intrinsic parameters. Together with the extrinsic parameters which are the luminosity distance d_L , the right

TABLE VIII: Parameter estimation for the new AresGW candidate events.

#	Event Name	\mathcal{M} (M_{\odot})	q	m_1 (M_{\odot})	m_2 (M_{\odot})	D_L (Mpc)	χ_{eff}	SNR (H1)	SNR (L1)	SNR $\hat{\rho}$ (network)
1	GW190511_125545	$28.95^{+9.45}_{-6.86}$	$0.72^{+0.25}_{-0.36}$	$40.7^{+16.2}_{-10.5}$	$28.2^{+11.6}_{-11.2}$	3707^{+3471}_{-2173}	$0.23^{+0.25}_{-0.29}$	2.29	7.34	7.29
2	GW190614_134749	$25.97^{+16.59}_{-6.20}$	$0.70^{+0.27}_{-0.36}$	$37.0^{+31.8}_{-11.7}$	$25.2^{+15.2}_{-9.7}$	6551^{+9562}_{-3558}	$0.05^{+0.34}_{-0.34}$	3.51	6.08	7.02
3	GW190607_083827	$30.48^{+7.21}_{-4.68}$	$0.78^{+0.19}_{-0.29}$	$40.5^{+12.0}_{-7.6}$	$31.0^{+9.1}_{-8.2}$	4928^{+2725}_{-2435}	$0.01^{+0.26}_{-0.30}$	4.04	7.29	8.33
4	GW190904_104631	$21.24^{+5.76}_{-4.40}$	$0.64^{+0.31}_{-0.33}$	$31.3^{+14.5}_{-8.5}$	$19.7^{+7.1}_{-7.2}$	5614^{+4441}_{-2864}	$0.05^{+0.30}_{-0.37}$	4.50	4.88	6.64
5	GW190523_085933	$23.82^{+10.24}_{-7.95}$	$0.49^{+0.45}_{-0.32}$	$41.7^{+19.3}_{-15.5}$	$19.4^{+14.6}_{-10.5}$	6091^{+6613}_{-3702}	$0.42^{+0.31}_{-0.45}$	3.48	5.14	6.02
6	GW200208_211609	$18.83^{+4.68}_{-3.18}$	$0.69^{+0.28}_{-0.40}$	$26.9^{+14.6}_{-6.3}$	$18.0^{+6.4}_{-6.9}$	3669^{+3413}_{-1985}	$0.01^{+0.37}_{-0.37}$	4.75	6.22	7.83
7	GW190705_164632	$27.21^{+7.34}_{-5.24}$	$0.52^{+0.41}_{-0.32}$	$44.7^{+24.8}_{-12.8}$	$23.0^{+11.7}_{-9.8}$	5692^{+4030}_{-2863}	$0.29^{+0.26}_{-0.34}$	4.42	6.88	8.11
8	GW190426_082124	$17.93^{+4.12}_{-3.42}$	$0.45^{+0.45}_{-0.28}$	$31.5^{+22.5}_{-11.3}$	$13.8^{+6.9}_{-5.2}$	3213^{+4555}_{-1573}	$-0.01^{+0.39}_{-0.50}$	5.15	4.46	6.41

ascension α and declination δ , the inclination ι of the system with respect to the observer's line of sight, the polarization angle ψ , the coalescence phase ϕ_c and time t_c , this amounts to a total of 15 parameters that were inferred. In Table VIII, we display only the main parameters inferred for each new candidate event: the source-frame chirp mass (\mathcal{M}), the component masses (m_1 and m_2), the mass ratio (q), the luminosity distance (D_L), the effective spin (χ_{eff}) and the reweighted network SNR ($\hat{\rho}$).

Based on the median values of the individual masses and the chirp mass, we find that all our new candidate events fall within the effective training data range of AresGW and are detected with an reweighted network SNR in the range $6.22 \leq \hat{\rho} \leq 8.33$. This range is not surprising. Other algorithms have already detected events with higher network SNR, which we have also confirmed in Section VI. Moreover, the other algorithms evaluate the data of each detector independently and impose a threshold on the individual SNR they consider acceptable. For some of our new events, with low SNR values at the Hanford detector, this could explain why these algorithms did not detect them. Note that most of the injections on which AresGW was trained had a single-detector SNR < 4 (see [73]), which explains the good sensitivity of AresGW to low-SNR signals. In Section VII C we analyze further the distribution of the network SNR for our new candidate events, compared to the events detected by other algorithms.

In Appendix A, we present corner plots of the 1-D and 2-D posterior distributions of the main parameters for all 8 new candidate events. The values shown for each 1-D distribution correspond to the median, along with the marginalized values for the 90% confidence interval. Since Bilby assumes a Gaussian likelihood, it is expected that the resulting posterior distributions will be Gaussian-like, in the absence of loud non-Gaussian noise features. Hence, a prominent Gaussian morphology of the posterior distributions favors the robustness of the parameter estimation. For all of our new candidate events, the Bayes factor was larger than unity.

In Fig. 20 we present the marginal posterior probability distributions corresponding to all 8 new candidate events in the form of violin plots. The morphology and

choice of the showcased parameters aligns with the respective version included in GWTC-3.

C. Population properties of new GW candidate events

In the following section, we will examine the distribution of various properties of our newly identified candidate events and compare them to the properties of previously published BBH merger events. We stress that we are only comparing *median* values, and one should take into account the uncertainties in the corresponding posterior distributions to arrive at quantitative statements.

The chirp mass distribution of BBH mergers, as inferred in [97], using observations in the GWTC-2 catalog [5], shows multiple peaks, starting around $8 M_{\odot}$. Beyond this primary peak, secondary peaks were inferred in [97] at approximately $14 M_{\odot}$ and $26 M_{\odot}$, while an outlier appeared at $\sim 45 M_{\odot}$. For further astrophysical considerations regarding the expected chirp mass distribution, see, e.g. [98].

By incorporating known events detected by both LIGO detectors, as reported in all previous catalogs (GWTC, OGC, and IAS), we obtain the histogram of chirp masses shown in Fig. 21. This distribution shows a mean of $29.13 M_{\odot}$, and the majority of events previously detected are distributed around this value. Additionally, there is a secondary peak for masses smaller than $10 M_{\odot}$, while the frequency of samples continuously decreases beyond the highest peak.

In Fig. 21 we also display the distribution of our new candidate events, which is Gaussian-like with a mean of $24.30 M_{\odot}$. This specific value can be attributed to two main factors. Firstly, the astrophysical distribution of the sources, as implied by the previously published events, appears to have a peak near this value. Additionally, AresGW likely became more sensitive around the mean of the training data, which closely aligns, by design, with this value. The fact that *our distribution aligns with that from the other catalogs* serves as a positive indicator for the astrophysical origin of our new candidate events. Similar conclusions can be drawn when one examines the distribution of the primary mass, m_1 ,

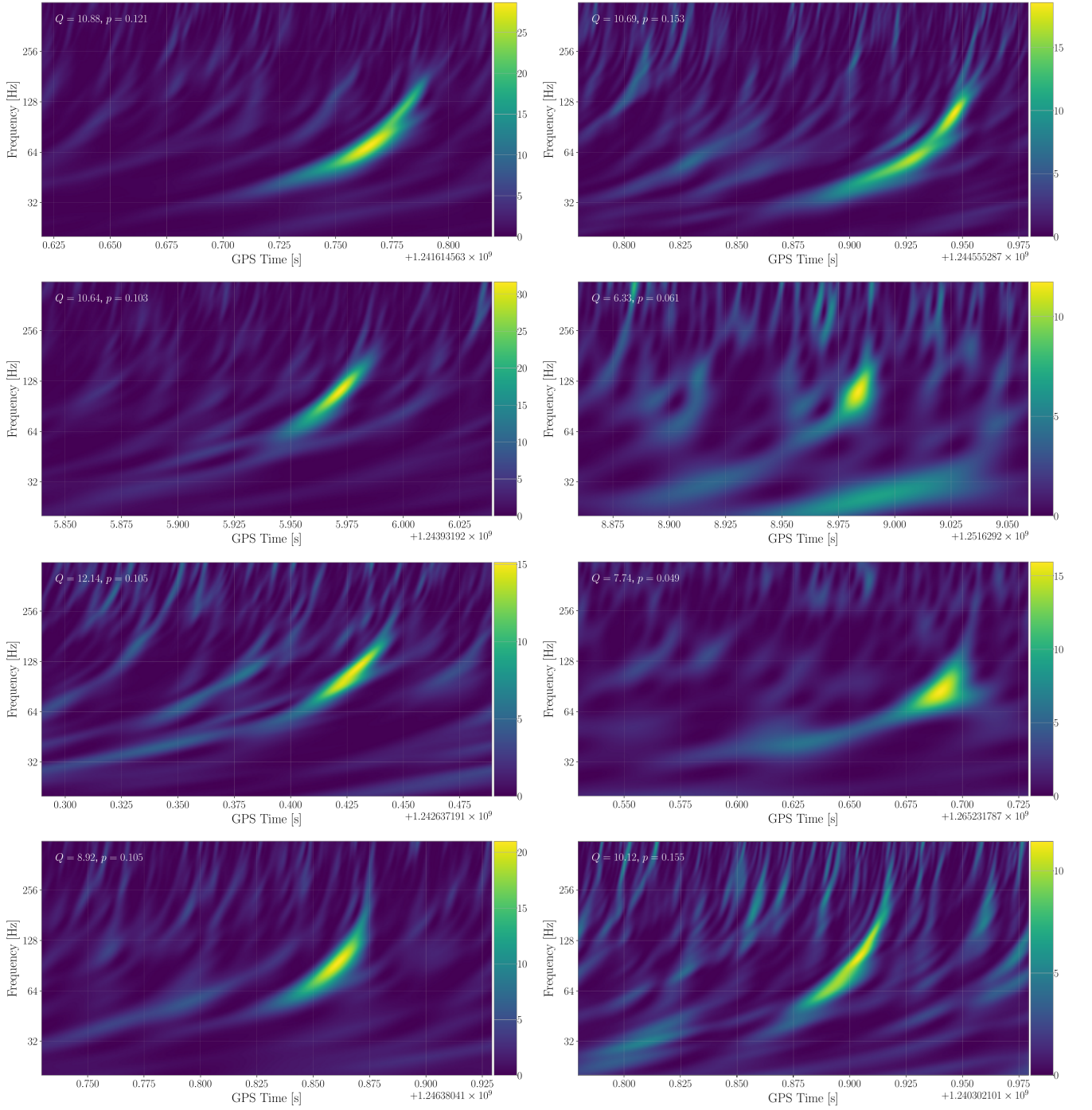


FIG. 19: Qp-transform spectrogram of the eight new candidate events identified by AresGW in Table VII. From left to right and top to bottom: 1st row: GW190511_125545 & GW190614_134749. 2nd row: GW190607_083827 & GW190904_104631. 3rd row: GW190523_085933 & GW200208_211609. 4th row: GW190705_164632 & GW190426_082124. All plots are for the LIGO Livingston detector, except for the last one, which is for the LIGO Hanford detector.

see Fig. 22.

Actually, the broad agreement between the distribution of the new AresGW candidate events and those previously detected by other algorithms is evident through

various comparisons. For example, in Fig. 23, the distribution of the chirp mass \mathcal{M} vs the mass ratio q for our new candidate events is in agreement with the corresponding distribution for most previously published

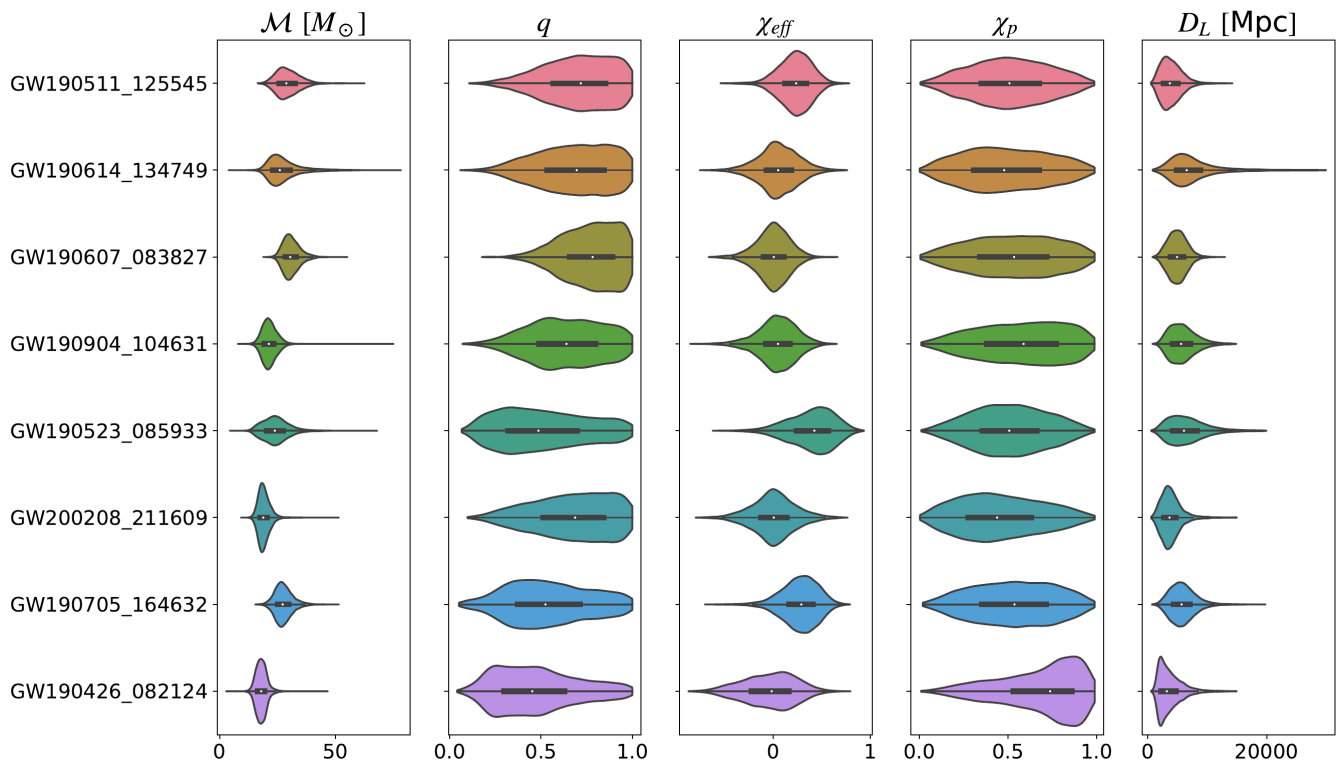


FIG. 20: Marginal probability distributions for the source chirp mass \mathcal{M} , mass ratio q , effective inspiral spin χ_{eff} , effective precession spin χ_p and luminosity distance D_L for the new candidate events identified by AresGW.

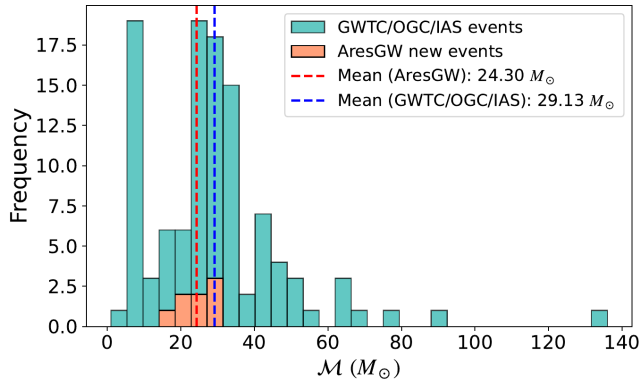


FIG. 21: Distribution of chirp masses (\mathcal{M}) for the new candidate events identified by AresGW (orange), compared to the corresponding distribution of previously published events (green).

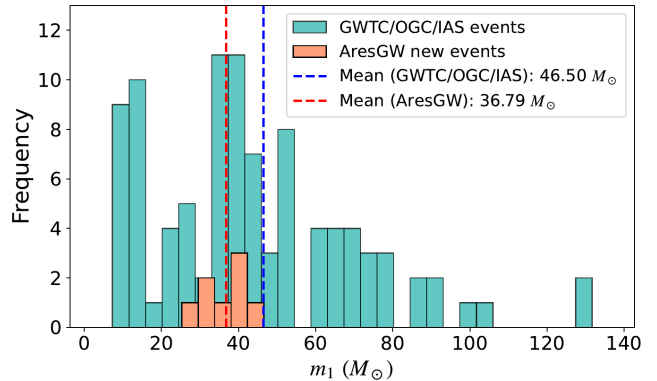


FIG. 22: Same as Fig. 21, but for m_1 .

events. Similarly, the chirp mass \mathcal{M} vs. effective spin χ_{eff} distribution of our new candidate events is comparable to the corresponding distribution of the events listed in the catalogs of the GWTC and OGC catalogs. The distribution of the IAS is wider, as depicted in Fig. 24.

However, our new candidate events exhibit some distinctive characteristics. For example, as illustrated in Fig. 25, our candidate events tend to exhibit higher luminosity distances D_L compared to the average of pre-

viously confirmed events. This observation underscores the high sensitive distance of AresGW.

The successful detection of distant, high-redshift black hole binaries can provide valuable insights into the evolution of their merger rate over different redshifts [99]. This can further support the potential correlation with other properties [100]. All of our new candidate events exceed the median value of $D_L \sim 3000$ Mpc for published GW events. Interestingly, our new candidate event GW190614_144749 constitutes the third most distant BBH merger ever detected in AresGW's effective training range.

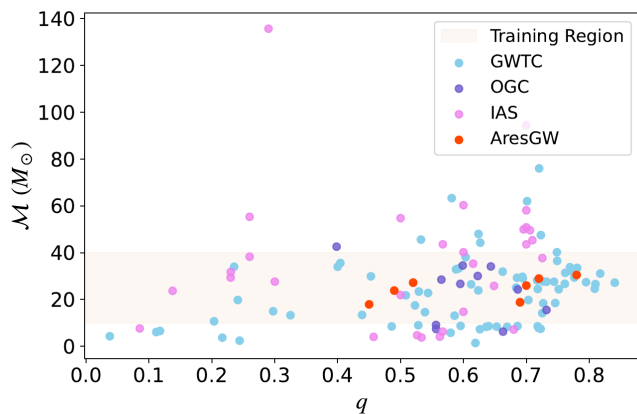


FIG. 23: Chirp mass \mathcal{M} vs. mass ratio q for the new candidate events identified by AresGW (red dots) in comparison to published events in the GWTC, OGC and IAS catalogs. The effective training region of AresGW is also shown.

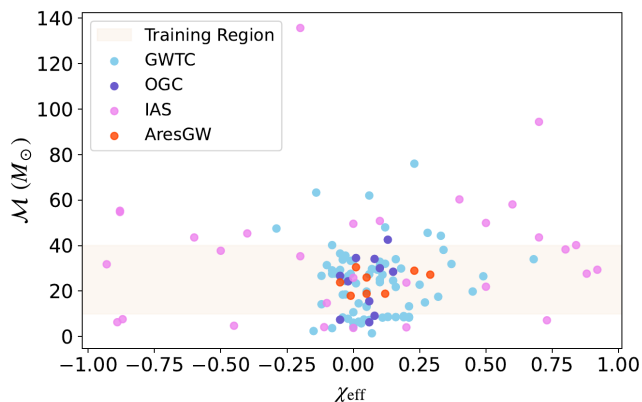


FIG. 24: Same as Fig. 23, but for the chirp mass \mathcal{M} vs. effective inspiral spin χ_{eff} .

Moreover, our new candidate events tend to have a lower reweighted network SNR $\hat{\rho}$ compared to those found in the GWTC, OGC, and IAS catalogs. As observed in Fig. 26, there is a general tendency for detected events to exhibit a higher FAR at lower SNR. The majority of our new candidate events follows this trend. However, our new candidate events can reach lower SNR compared to other algorithms, while maintaining a comparable FAR.

This observation suggests that, although our new candidate events have a relatively low signal-to-noise ratio, our ML-based detection pipeline has effectively detected them. This increased sensitivity and efficacy in event detection distinguish AresGW from traditional detection algorithms.

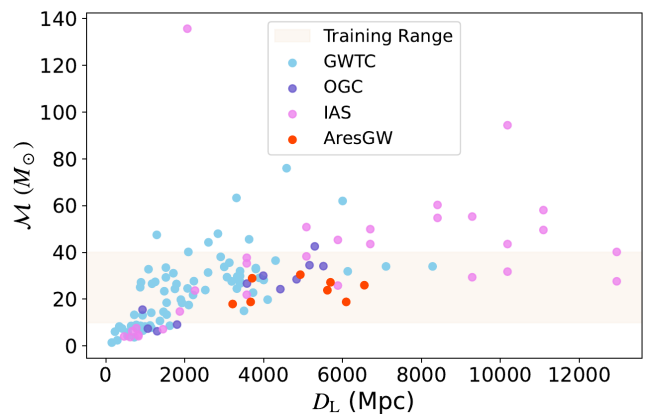


FIG. 25: Same as Fig. 23, but for the chirp mass \mathcal{M} vs. luminosity distance D_L .

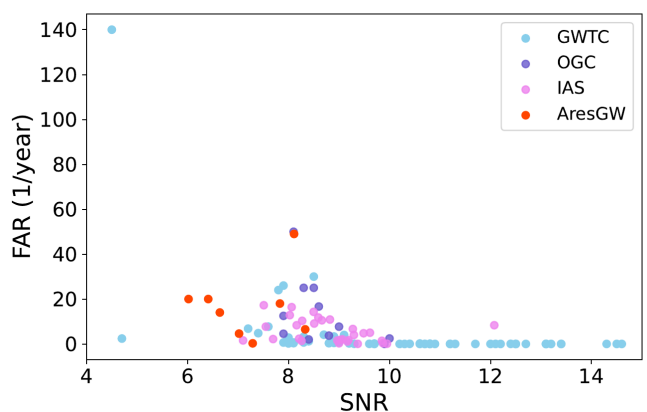


FIG. 26: False alarm rate vs. signal-to-noise ratio for the new candidate events identified by AresGW (red dots) in comparison to published events in the GWTC, OGC and IAS catalogs.

VIII. CONCLUSIONS AND DISCUSSION

The AresGW neural network has undergone enhancements, including the utilization of a larger dataset for training, double precision for results, and a 350 Hz low-pass filter for both training and detection. Furthermore, the development of new filters for data analysis, coupled with the implementation of glitch removal techniques, utilizing the capabilities of Gravity Spy, has resulted in the categorization of triggers into three distinct classes: Default Low-pass, Selective Noise Rejection, and Selective Passband triggers. The second and third classes employ different filters, such as noise filters of high-frequency cut-offs at 400 Hz or 500 Hz, to reduce false alarms. As a result, false alarms were reduced by at least 70% in the first class and 90% in the second class, when compared to false alarms in the first class alone.

AresGW utilizes two input channels and is trained on BBH merger signal injections in O3a noise from the two

LIGO detectors. In the effective training range, we considered events detected when both the Livingston and Hanford detectors were operational during the O3 period, with source masses in the range $m_{1,2} \in (7M_{\odot}, 50M_{\odot})$ and chirp mass in the range $\mathcal{M} \in (10M_{\odot}, 40M_{\odot})$. With the aforementioned improvements, AresGW successfully confirmed 34 of the 43 signals in its effective training range, that were previously detected by the GWTC, OGC, or IAS algorithms. The four out of the nine undetected signals had a rather low published astrophysical probability of $p_{\text{astro}} \leq 0.63$.

Beyond the confines of the training dataset, a total of 55 detections were recorded when both LIGO detectors were active. Our algorithm identified 10 of these detections with $p_{\text{astro}} \geq 0.99$, showcasing the resilience of our neural network in detecting gravitational wave signals even beyond its training dataset. This underscores the potential for AresGW to maintain high sensitivity in various mass ranges with appropriate training.

In addition to identifying published events in the GWTC, OGC, and IAS catalogs, our machine algorithm detected 8 new gravitational wave candidate events within its effective training range. With the addition of these new candidate events, AresGW reached a total of 42 detections in its effective training range, making AresGW the most efficient detection pipeline in this range. Parameter estimation for all these signals was performed using Bilby, while the appropriate time and consistency tests were also successfully passed.

Furthermore, we compared our new candidate events with previously detected signals and found that their distribution aligns with those from other catalogs, a positive indicator that our new candidate events are likely of astrophysical origin. A distinctive characteristic of these new events is that they exhibit luminosity distances higher than the average value for previously confirmed events, further highlighting the sensitivity of AresGW. Furthermore, our new candidate events tend to have a lower signal-to-noise ratio than previously detected signals. Here again, our pipeline distinguishes itself by reaching lower signal-to-noise ratio levels at a false alarm rate comparable to other algorithms.

AresGW also confirms several events with high astrophysical probabilities: GW190916_200658, originally detected by mbta with $p_{\text{astro}} = 0.66$ and by pycbc_bbh with $p_{\text{astro}} = 0.65$, now confirmed with $p_{\text{astro}} = 1.00$; GW200305_084739, found by OGC with $p_{\text{astro}} = 0.59$, is now confirmed with $p_{\text{astro}} = 1.00$; GW190906_054335, detected by IAS with $p_{\text{astro}} = 0.61$, is now confirmed with $p_{\text{astro}} = 0.99$; and GW200106_134123, found by OGC with $p_{\text{astro}} = 0.69$, is now confirmed with $p_{\text{astro}} = 0.95$.

Moreover, to evaluate the adaptability of AresGW, we also applied it on data in which the Virgo detector was operational at the same time of one of the other two LIGO detectors, without any retraining. Our findings show that AresGW can adapt to Virgo’s noise characteristics and, when coupled with an additional detector, it effectively identifies signals buried in noise. In fact,

AresGW successfully detected five of the eight events in the data with a ranking statistic ($\langle \mathcal{R}_s \rangle$) exceeding 3.5 (the threshold used in the analysis presented above). This underscores once again the significant generalizability of our network.

The analysis of AresGW’s adaptability to Virgo’s noise led us to investigate its generalization capacity by testing it on data from the O1 and O2 observing periods, too. Our results revealed that our machine learning code successfully validated all, but one, events previously detected during O2, achieving a maximum value ($\langle \mathcal{R}_s \rangle$) of 16.0. It also identified the inaugural gravitational wave event, GW150914, from the O1 period with the same ranking statistic. This indicates that AresGW effectively detected almost all events within its training range in both O1 and O2 periods. Notably, the neural network’s ability to generalize effectively also on data from those observing periods underscores its generalization capability, suggesting the potential for detecting new gravitational waves in O1 and O2 data without necessarily retraining AresGW, as well as its potential applicability to various phenomena characterized by time series with non-Gaussian noise. Furthermore, this bodes well for the O4 observing run, anticipated to benefit from significantly reduced noise levels in the LIGO detectors.

Looking ahead, there are several avenues to further advance the capabilities of the AresGW neural network. For example, retraining AresGW on the noise characteristics of each observing run could enhance its adaptability and detection efficiency. Another avenue for exploration lies in training the algorithm on different combinations of detectors, including single, double, and triple detector setups. In particular, the implementation of a three-channel AresGW pipeline holds significant promise, as it would leverage data from multiple detectors to improve detection accuracy and reduce false alarms. Furthermore, directly integrating glitch identification in AresGW, could help mitigate false positives by excluding glitches from trigger selections.

Additionally, the utilization of a four-channel network, incorporating both time series and spectrogram data, presents an intriguing opportunity to enhance the algorithm’s sensitivity and precision. By training the network to dynamically adjust low-pass filters based on spectrogram analysis, we could potentially optimize detection thresholds for various signal segments, further refining AresGW’s performance in capturing gravitational wave events.

Moreover, one more promising avenue is to extend the application of AresGW to the detection of gravitational waves emitted from the merger of compact binary systems involving at least one neutron star, to supernovae, and other astrophysical events. Neutron star mergers, in particular, are of significant interest, due to their potential to produce observable electromagnetic counterparts, known as kilonovae, enabling multimessenger studies.

IX. ACKNOWLEDGEMENTS

We are grateful to Thomas Dent, Melissa Lopez and Viola Sordini for useful discussions. We are indebted to Derek Davis, Thomas Dent and Agata Trogato for detailed comments that improved the manuscript. We are also grateful to Andrea Virtuoso and Edoardo Milotti, for making their Qp-transform code publicly available and to the organizers of the MLGWSC-1 challenge, for providing routines for creating different datasets. We acknowledge the support provided by the IT Center of the Aristotle University of Thessaloniki (AUTH) as our results have been produced using the AUTH High-Performance Computing Infrastructure and Resources. We also acknowledge support from COST Action (European Cooperation in Science and Technology) CA17137 (G2Net). This research has made use of data or software obtained from the Gravitational Wave Open Science Center (gw-openscience.org), a service of LIGO Laboratory, the LIGO Scientific Collaboration, the Virgo Collaboration, and KAGRA. LIGO Laboratory and Advanced LIGO are funded by the United States National Science Foundation (NSF) as well as the Science and Technology Facilities Council (STFC) of the United Kingdom, the Max-Planck-Society (MPS), and the State of Niedersachsen/Germany for support of the construction of Advanced LIGO and construction and operation of the GEO600 detector. Additional support for Advanced LIGO was provided by the Australian Research Council. Virgo is funded, through the European Gravitational Observatory (EGO), by the French Centre National de Recherche Scientifique (CNRS), the Italian Istituto Nazionale di Fisica Nucleare (INFN) and the Dutch Nikhef, with contributions by institutions from Belgium, Germany, Greece, Hungary, Ireland, Japan, Monaco, Poland, Portugal, Spain. The construction and operation of KAGRA are funded by Ministry of Education, Culture, Sports, Science and Technology (MEXT), and Japan Society for the Promotion of Science (JSPS), National Research Foundation (NRF) and Ministry of Science and ICT (MSIT) in Korea, Academia Sinica (AS) and the Ministry of Science and Technology (MoST) in Taiwan.

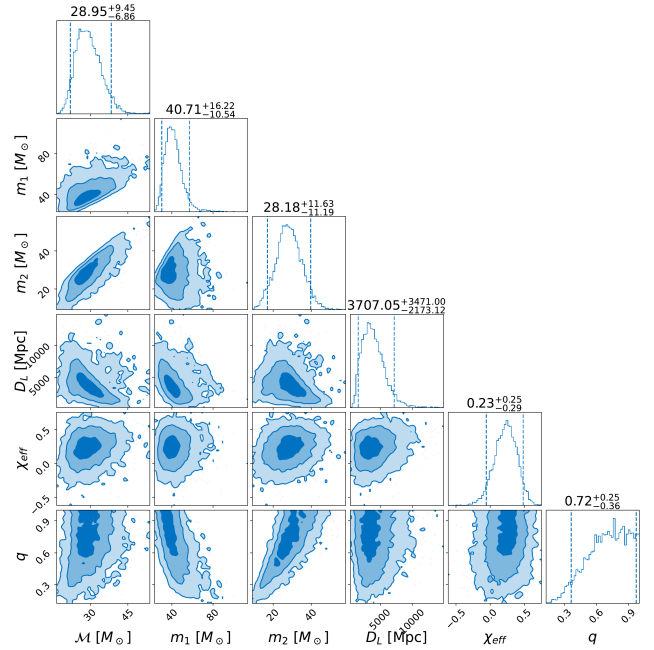


FIG. 27: 1-D and 2-D Marginal Posterior Distributions corresponding to the inferred parameters of the new event GW190511_125545, identified by AresGW.

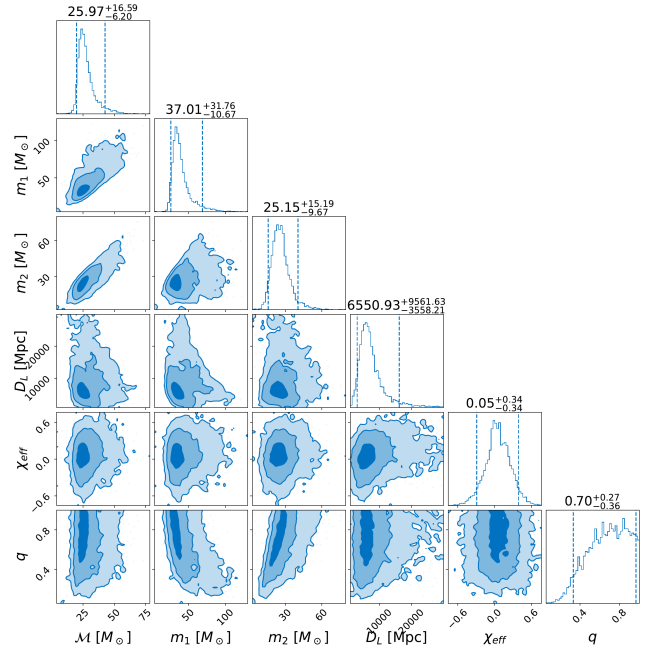


FIG. 28: Same as Fig. 27, but for the new event GW190614_134749.

Appendix A: Corner Plots of AresGW New Detections

Figs. 27 – 34 display corner plots of the most important parameters for the 8 new GW candidate events, identified by AresGW.

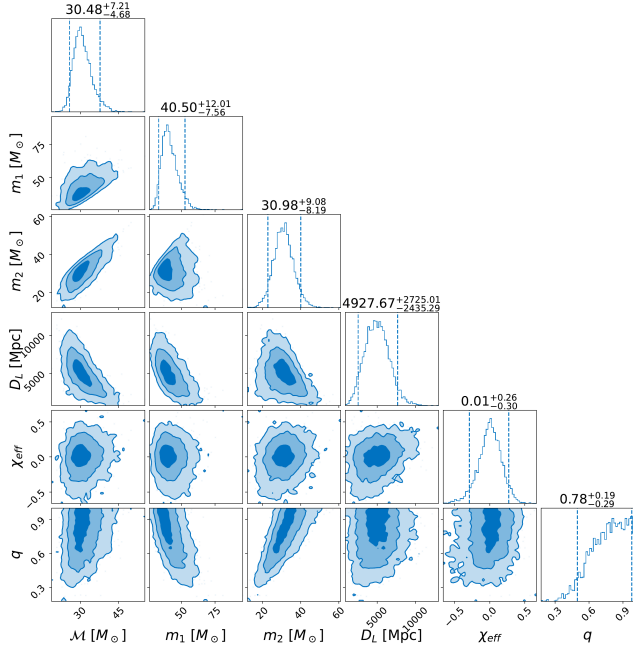


FIG. 29: Same as Fig. 27, but for the new event GW190607_083827.

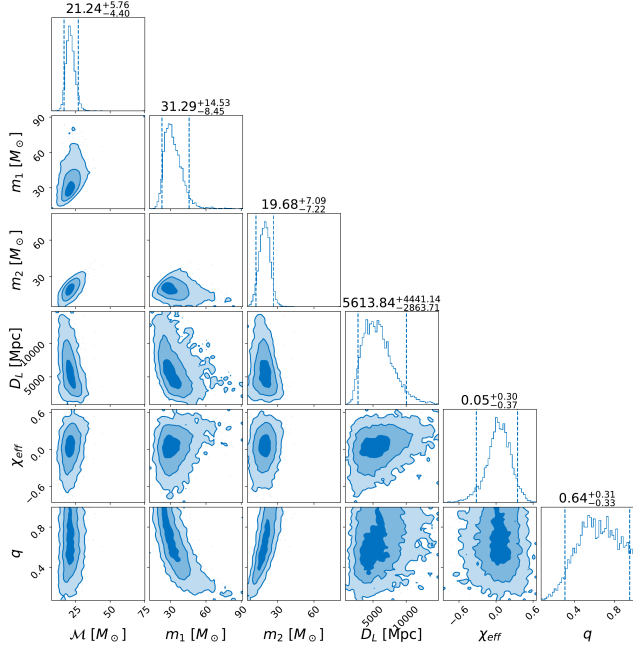


FIG. 30: Same as Fig. 27, but for the new event GW190904_104631.

Appendix B: Time-Domain Reconstruction of AresGW New Detections

To provide further visual context, we present the time-series data from both LIGO detectors for the 16 new

detections made by AresGW in Figs. 35-42. In these figures, the whitened data are depicted in orange, the re-

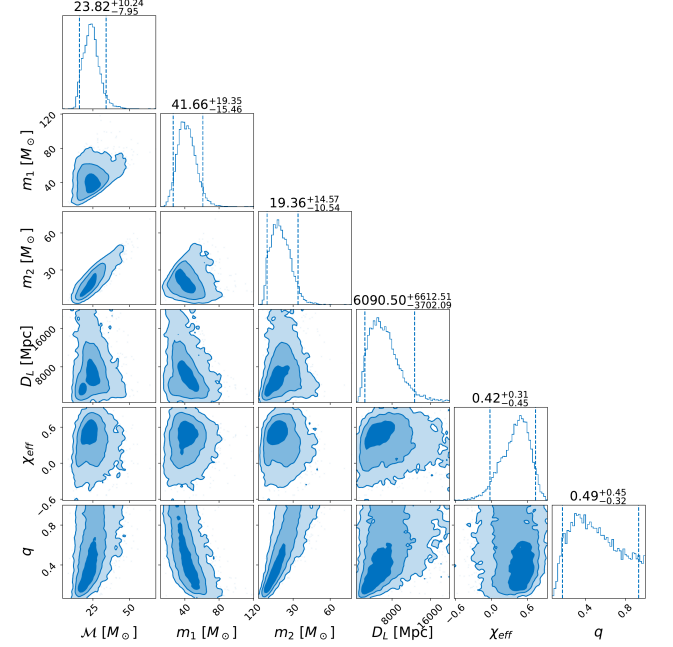


FIG. 31: Same as Fig. 27, but for the new event GW190523_085933.

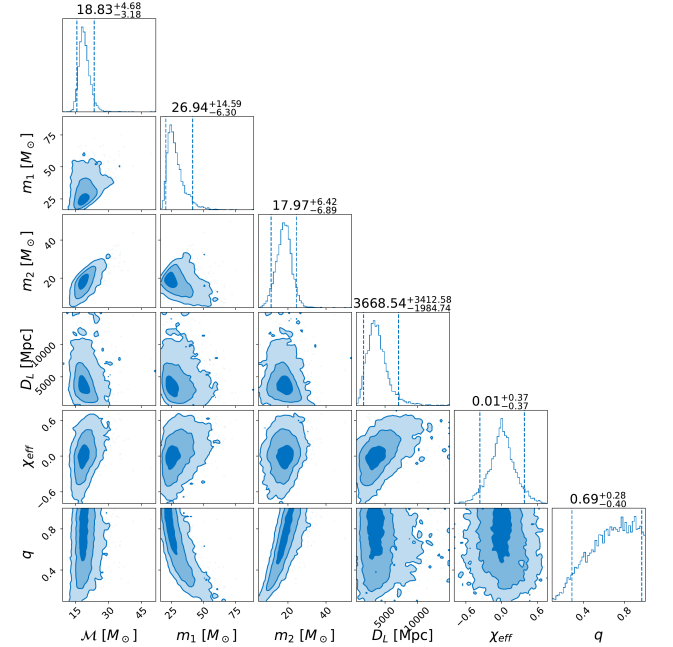


FIG. 32: Same as Fig. 27, but for the new event GW200208_211609.

constructed whitened-bandpassed median waveforms in blue, and their corresponding 90% confidence intervals in light blue. Additionally, the frequency band used is indicated in the upper right corner of each figure.

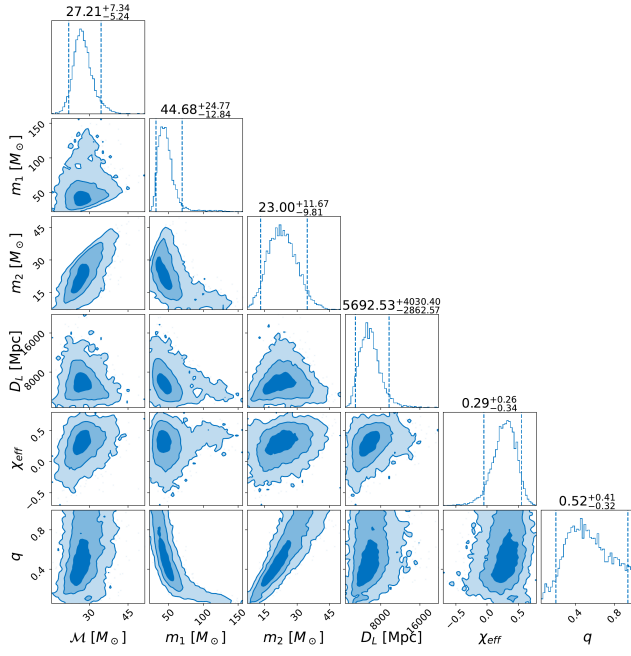


FIG. 33: Same as Fig. 27, but for the new event GW190705_164632.

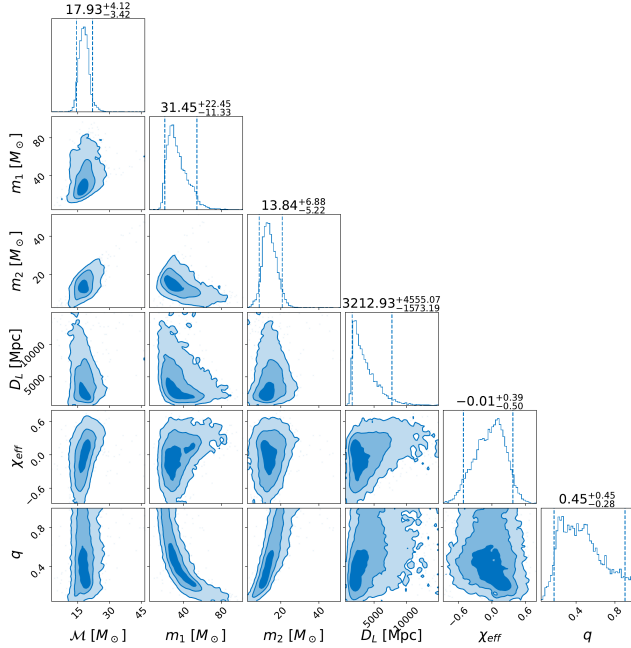


FIG. 34: Same as Fig. 27, but for the new event GW190426_082124.

- [1] J. Aasi *et al.* (LIGO Scientific Collaboration), Advanced LIGO, *Classical and Quantum Gravity* **32**, 074001 (2015).
 [2] F. Acernese *et al.* (Virgo Collaboration), Advanced Virgo: a second-generation interferometric gravitational

- wave detector, *Classical and Quantum Gravity* **32**, 024001 (2014).
 [3] T. Akutsu *et al.*, Overview of KAGRA: Detector design and construction history, *Progress of Theoretical and Experimental Physics* **2021**, 10.1093/ptep/ptaa125

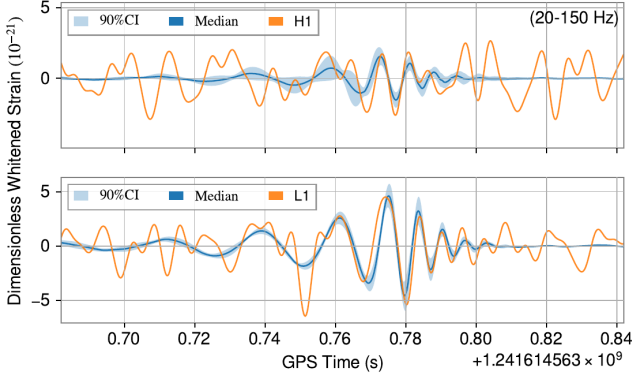


FIG. 35: Whiten, bandpassed strain data and reconstructed waveform for the new event GW190511_12545 identified by AresGW.

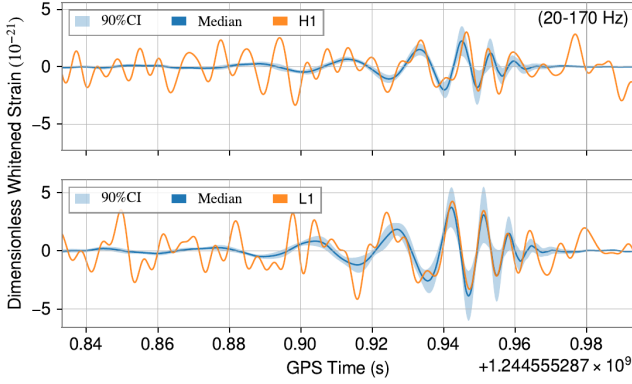


FIG. 36: Same as Fig. 35, but for the new event GW190614_134749.

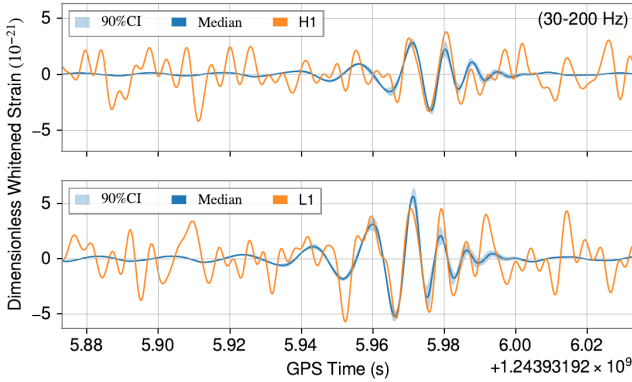


FIG. 37: Same as Fig. 35, but for the new event GW190607_083827.

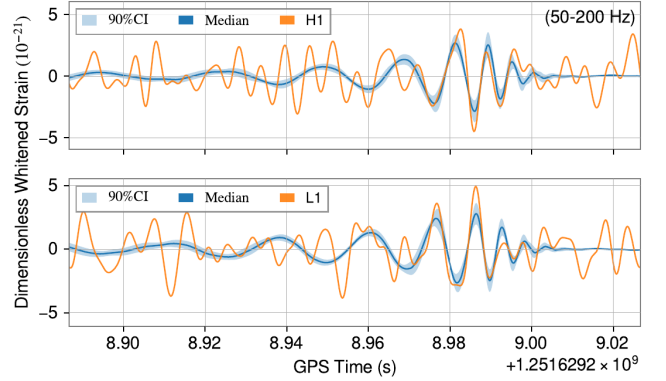


FIG. 38: Same as Fig. 35, but for the new event GW190904_104631.

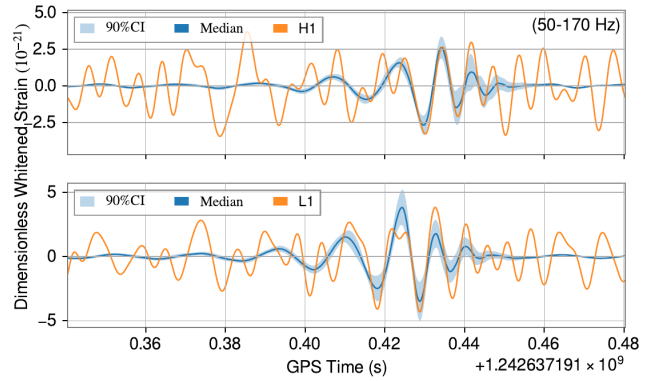


FIG. 39: Same as Fig. 35, but for the new event GW190523_085933.

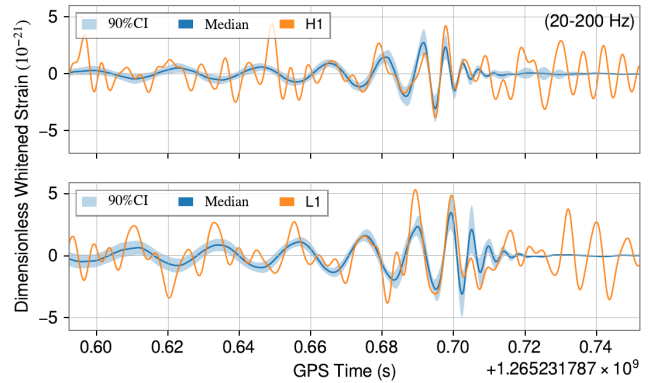


FIG. 40: Same as Fig. 35, but for the new event GW200208_211609.

(2020), 05A101.

- [4] B. P. Abbott *et al.* (LIGO Scientific Collaboration and Virgo Collaboration), Gwtc-1: A gravitational-wave transient catalog of compact binary mergers observed by ligo and virgo during the first and second observing runs, *Phys. Rev. X* **9**, 031040 (2019).

- [5] R. Abbott *et al.* (LIGO Scientific Collaboration and Virgo Collaboration), GWTC-2: Compact Binary Coalescences Observed by LIGO and Virgo During the First Half of the Third Observing Run, *Phys. Rev. X* **11**, 021053 (2021).
- [6] LIGO Scientific Collaboration and Virgo Collaboration, GWTC-2.1: Deep extended catalog of compact binary

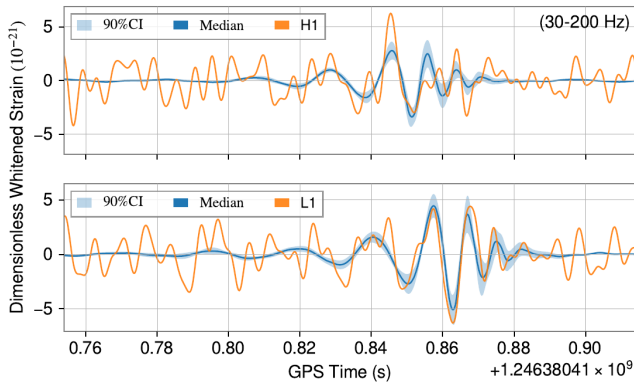


FIG. 41: Same as Fig. 35, but for the new event GW190705_164632.

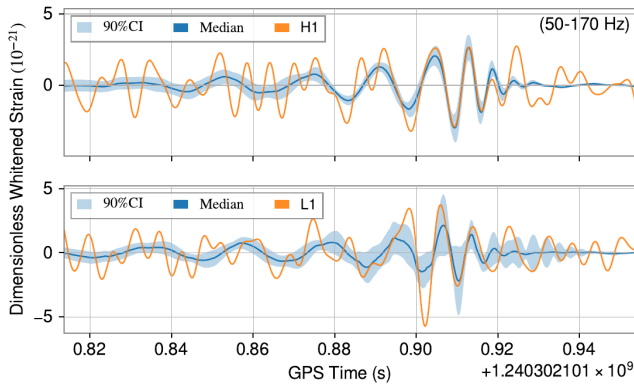


FIG. 42: Same as Fig. 35, but for the new event GW190426_082124.

coalescences observed by LIGO and Virgo during the first half of the third observing run - parameter estimation data release (version v2) (2022).

- [7] R. Abbott *et al.* (The LIGO Scientific Collaboration and the Virgo Collaboration and the KAGRA Collaboration), GWTC-3: Compact Binary Coalescences Observed by LIGO and Virgo During the Second Part of the Third Observing Run, arXiv e-prints , arXiv:2111.03606 (2021).
- [8] A. H. Nitz, C. Capano, A. B. Nielsen, S. Reyes, R. White, D. A. Brown, and B. Krishnan, 1-OGC: The First Open Gravitational-wave Catalog of Binary Mergers from Analysis of Public Advanced LIGO Data, *Astrophys. J.* **872**, 195 (2019).
- [9] A. H. Nitz, T. Dent, G. S. Davies, S. Kumar, C. D. Capano, I. Harry, S. Mozzon, L. Nuttall, A. Lundgren, and M. Tápai, 2-OGC: Open Gravitational-wave Catalog of Binary Mergers from Analysis of Public Advanced LIGO and Virgo Data, *Astrophys. J.* **891**, 123 (2020).
- [10] A. H. Nitz, C. D. Capano, S. Kumar, Y.-F. Wang, S. Kastha, M. Schäfer, R. Dhurkunde, and M. Cabero, 3-OGC: Catalog of Gravitational Waves from Compact-binary Mergers, *Astrophys. J.* **922**, 76 (2021).
- [11] A. H. Nitz, S. Kumar, Y.-F. Wang, S. Kastha, S. Wu, M. Schäfer, R. Dhurkunde, and C. D. Capano, 4-OGC:

Catalog of Gravitational Waves from Compact Binary Mergers, *Astrophys. J.* **946**, 59 (2023).

- [12] S. Olsen, T. Venumadhav, J. Mushkin, J. Roulet, B. Zackay, and M. Zaldarriaga, New binary black hole mergers in the LIGO-Virgo O3a data, *Phys. Rev. D* **106**, 043009 (2022).
- [13] A. K. Mehta, S. Olsen, D. Wadekar, J. Roulet, T. Venumadhav, J. Mushkin, B. Zackay, and M. Zaldarriaga, New binary black hole mergers in the LIGO-Virgo O3b data, arXiv e-prints , arXiv:2311.06061 (2023).
- [14] D. Wadekar, J. Roulet, T. Venumadhav, A. K. Mehta, B. Zackay, J. Mushkin, S. Olsen, and M. Zaldarriaga, New black hole mergers in the LIGO-Virgo O3 data from a gravitational wave search including higher-order harmonics, arXiv e-prints , arXiv:2312.06631 (2023).
- [15] P. Kumar and T. Dent, Optimized Search for a Binary Black Hole Merger Population in LIGO-Virgo O3 Data, arXiv e-prints , arXiv:2403.10439 (2024).
- [16] M. Saleem *et al.*, The science case for LIGO-India, *Classical and Quantum Gravity* **39**, 025004 (2022).
- [17] R. X. Adhikari *et al.* (LIGO), A cryogenic silicon interferometer for gravitational-wave detection, *Class. Quant. Grav.* **37**, 165003 (2020).
- [18] D. Reitze, R. X. Adhikari, S. Ballmer, B. Barish, L. Barsotti, G. Billingsley, D. A. Brown, Y. Chen, D. Coyne, R. Eisenstein, M. Evans, P. Fritschel, E. D. Hall, A. Lazzarini, G. Lovelace, J. Read, B. S. Sathyaprakash, D. Shoemaker, J. Smith, C. Torrie, S. Vitale, R. Weiss, C. Wipf, and M. Zucker, Cosmic Explorer: The U.S. Contribution to Gravitational-Wave Astronomy beyond LIGO, in *Bulletin of the American Astronomical Society*, Vol. 51 (2019) p. 35, arXiv:1907.04833 [astro-ph.IM].
- [19] M. Maggiore, C. Van Den Broeck, N. Bartolo, E. Belgacem, D. Bertacca, M. A. Bizouard, M. Branchesi, S. Clesse, S. Foffa, J. García-Bellido, S. Grimm, J. Harms, T. Hinderer, S. Matarrese, C. Palomba, M. Peloso, A. Ricciardone, and M. Sakellariadou, Science case for the Einstein telescope, *Journal of Cosmology and Astroparticle Physics* **2020** (3), 050.
- [20] K. Ackley *et al.*, Neutron Star Extreme Matter Observatory: A kilohertz-band gravitational-wave detector in the global network, *Publ. Astron. Soc. Austral.* **37**, e047 (2020).
- [21] P. Couvares, I. Bird, E. Porter, S. Bagnasco, M. Punturo, D. Reitze, S. Katsanevas, T. Kajita, V. Kalogera, H. Lueck, D. McClelland, S. Rowan, G. Sanders, B. S. Sathyaprakash, D. Shoemaker, and J. van den Brand, Gravitational Wave Data Analysis: Computing Challenges in the 3G Era, arXiv e-prints , arXiv:2111.06987 (2021).
- [22] E. Cuoco, J. Powell, M. Cavaglià, K. Ackley, M. Berger, C. Chatterjee, M. Coughlin, S. Coughlin, P. Easter, R. Essick, H. Gabbard, T. Gebhard, S. Ghosh, L. Haegel, A. Iess, D. Keitel, Z. Márka, S. Márka, F. Morawski, T. Nguyen, R. Ormiston, M. Pürrer, M. Razzano, K. Staats, G. Vajente, and D. Williams, Enhancing gravitational-wave science with machine learning, *Machine Learning: Science and Technology* **2**, 011002 (2020).
- [23] V. Benedetto, F. Gissi, G. Ciaparrone, and L. Troiano, Ai in gravitational wave analysis, an overview, *Applied Sciences* **13**, 10.3390/app13179886 (2023).

- [24] T. Zhao, R. Shi, Y. Zhou, Z. Cao, and Z. Ren, Dawning of a New Era in Gravitational Wave Data Analysis: Unveiling Cosmic Mysteries via Artificial Intelligence – A Systematic Review, arXiv e-prints , arXiv:2311.15585 (2023).
- [25] H. Gabbard, M. Williams, F. Hayes, and C. Messenger, Matching matched filtering with deep networks for gravitational-wave astronomy, *Phys. Rev. Lett.* **120**, 141103 (2018).
- [26] D. George and E. A. Huerta, Deep neural networks to enable real-time multimessenger astrophysics, *Phys. Rev. D* **97**, 044039 (2018).
- [27] T. D. Gebhard, N. Kilbertus, I. Harry, and B. Schölkopf, Convolutional neural networks: A magic bullet for gravitational-wave detection?, *Phys. Rev. D* **100**, 063015 (2019).
- [28] R. Corizzo, M. Ceci, E. Zdravevski, and N. Japkowicz, Scalable auto-encoders for gravitational waves detection from time series data, *Expert Systems with Applications* **151**, 113378 (2020).
- [29] M. B. Schäfer, F. Ohme, and A. H. Nitz, Detection of gravitational-wave signals from binary neutron star mergers using machine learning, *Phys. Rev. D* **102**, 063015 (2020).
- [30] H. Wang, S. Wu, Z. Cao, X. Liu, and J.-Y. Zhu, Gravitational-wave signal recognition of LIGO data by deep learning, *Phys. Rev. D* **101**, 104003 (2020).
- [31] P. G. Krastev, Real-time detection of gravitational waves from binary neutron stars using artificial neural networks, *Physics Letters B* **803**, 135330 (2020).
- [32] V. Skliris, M. R. K. Norman, and P. J. Sutton, Real-Time Detection of Unmodelled Gravitational-Wave Transients Using Convolutional Neural Networks, arXiv e-prints , arXiv:2009.14611 (2020).
- [33] Y.-C. Lin and J.-H. P. Wu, Detection of gravitational waves using Bayesian neural networks, *Phys. Rev. D* **103**, 063034 (2021).
- [34] H. Dodia, Detecting residues of cosmic events using residual neural network, in *2021 IEEE 17th International Conference on Intelligent Computer Communication and Processing (ICCP)* (2021) pp. 179–186.
- [35] E. A. Huerta, A. Khan, X. Huang, M. Tian, M. Levental, R. Chard, W. Wei, M. Heflin, D. S. Katz, V. Kindratenko, D. Mu, B. Blaiszik, and I. Foster, Accelerated, scalable and reproducible AI-driven gravitational wave detection, *Nature Astronomy* **5**, 1062 (2021).
- [36] T. Marianer, D. Poznanski, and J. X. Prochaska, A semisupervised machine learning search for never-seen gravitational-wave sources, *Mon. Not. R. Astr. Soc.* **500**, 5408 (2021).
- [37] W. Wei, A. Khan, E. A. Huerta, X. Huang, and M. Tian, Deep learning ensemble for real-time gravitational wave detection of spinning binary black hole mergers, *Physics Letters B* **812**, 136029 (2021).
- [38] J. D. Álvares, J. A. Font, F. F. Freitas, O. G. Freitas, A. P. Morais, S. Nunes, A. Onofre, and A. Torres-Forné, Exploring gravitational-wave detection and parameter inference using deep learning methods, *Classical and Quantum Gravity* **38**, 155010 (2021).
- [39] S. Jadhav, N. Mukund, B. Gadre, S. Mitra, and S. Abraham, Improving significance of binary black hole mergers in Advanced LIGO data using deep learning: Confirmation of GW151216, *Phys. Rev. D* **104**, 064051 (2021).
- [40] P. Chaturvedi, A. Khan, M. Tian, E. A. Huerta, and H. Zheng, Inference-optimized ai and high performance computing for gravitational wave detection at scale, *Frontiers in Artificial Intelligence* **5**, 10.3389/frai.2022.828672 (2022).
- [41] S. Choudhary, A. More, S. Suyamprakasam, and S. Bose, SiGMA-Net: Deep learning network to distinguish binary black hole signals from short-duration noise transients, arXiv e-prints , arXiv:2202.08671 (2022).
- [42] M. B. Schäfer and A. H. Nitz, From one to many: A deep learning coincident gravitational-wave search, *Phys. Rev. D* **105**, 043003 (2022).
- [43] F. P. Barone, D. Dell’Aquila, and M. Russo, A Novel Multi-Layer Modular Approach for Real-Time Gravitational-Wave Detection, arXiv e-prints , arXiv:2206.06004 (2022).
- [44] M. B. Schäfer, O. Zelenka, A. H. Nitz, F. Ohme, and B. Brügmann, Training strategies for deep learning gravitational-wave searches, *Physical Review D* **105**, 043002 (2022).
- [45] G. Baltus, J. Janquart, M. Lopez, H. Narola, and J.-R. Cudell, Convolutional neural network for gravitational-wave early alert: Going down in frequency, *Phys. Rev. D* **106**, 042002 (2022).
- [46] M. Andrews, M. Paulini, L. Sellers, A. Bobrick, G. Martire, and H. Vestal, DeepSNR: A deep learning foundation for offline gravitational wave detection, arXiv e-prints , arXiv:2207.04749 (2022).
- [47] C. Verma, A. Reza, G. Gaur, D. Krishnaswamy, and S. Caudill, Can Convolution Neural Networks Be Used for Detection of Gravitational Waves from Preprocessing Black Hole Systems?, arXiv e-prints , arXiv:2206.12673 (2022).
- [48] J. Aveiro, F. F. Freitas, M. Ferreira, A. Onofre, C. Providência, G. Gonçalves, and J. A. Font, Identification of binary neutron star mergers in gravitational-wave data using object-detection machine learning models, *Phys. Rev. D* **106**, 084059 (2022).
- [49] W. Guo, D. Williams, I. S. Heng, H. Gabbard, Y.-B. Bae, G. Kang, and Z.-H. Zhu, Mimicking mergers: mistaking black hole captures as mergers, *MNRAS* **516**, 3847 (2022).
- [50] M. Andrés-Carcasona, A. Menéndez-Vázquez, M. Martínez, and L. M. Mir, Searches for mass-asymmetric compact binary coalescence events using neural networks in the LIGO/Virgo third observation period, *Phys. Rev. D* **107**, 082003 (2023).
- [51] W. Alhassan, T. Bulik, and M. Suchenek, Detection of Einstein telescope gravitational wave signals from binary black holes using deep learning, *MNRAS* **519**, 3843 (2023).
- [52] J. Langendorff, A. Kolmus, J. Janquart, and C. Van Den Broeck, Normalizing Flows as an Avenue to Studying Overlapping Gravitational Wave Signals, *Phys. Rev. Lett.* **130**, 171402 (2023).
- [53] M. Dax, S. R. Green, J. Gair, M. Pürrer, J. Wildberger, J. H. Macke, A. Buonanno, and B. Schölkopf, Neural Importance Sampling for Rapid and Reliable Gravitational-Wave Inference, *Phys. Rev. Lett.* **130**, 171403 (2023).
- [54] S. Bini, G. Vedovato, M. Drago, F. Salemi, and G. A. Prodi, An autoencoder neural network integrated into gravitational-wave burst searches to improve the rejection of noise transients, *Classical and Quantum Gravity*

- 40**, 135008 (2023).
- [55] M. Tian, E. A. Huerta, and H. Zheng, Physics-inspired spatiotemporal-graph AI ensemble for gravitational wave detection, arXiv e-prints , arXiv:2306.15728 (2023).
- [56] C. Murali and D. Lumley, Detecting and denoising gravitational wave signals from binary black holes using deep learning, *Phys. Rev. D* **108**, 043024 (2023).
- [57] P. Bacon, A. Trovato, and M. Bejger, Denoising gravitational-wave signals from binary black holes with a dilated convolutional autoencoder, *Machine Learning: Science and Technology* **4**, 035024 (2023).
- [58] A. McLeod, D. Jacobs, C. Chatterjee, L. Wen, and F. Panther, Rapid Mass Parameter Estimation of Binary Black Hole Coalescences Using Deep Learning, arXiv e-prints , arXiv:2201.11126 (2022).
- [59] R. Qiu, P. G. Krastev, K. Gill, and E. Berger, Deep learning detection and classification of gravitational waves from neutron star-black hole mergers, *Physics Letters B* **840**, 137850 (2023).
- [60] H.-Y. Liu and Y.-T. Wang, Self-supervised learning for gravitational wave signal identification, arXiv e-prints , arXiv:2302.00295 (2023).
- [61] S.-J. Jin, Y.-X. Wang, T.-Y. Sun, J.-F. Zhang, and X. Zhang, Rapid identification of time-frequency domain gravitational wave signals from binary black holes using deep learning, arXiv e-prints , arXiv:2305.19003 (2023).
- [62] T. Fernandes, S. Vieira, A. Onofre, J. Calderón Bustillo, A. Torres-Forné, and J. A. Font, Convolutional neural networks for the classification of glitches in gravitational-wave data streams, *Classical and Quantum Gravity* **40**, 195018 (2023).
- [63] O. Gramaxo Freitas, J. Calderón Bustillo, J. A. Font, S. Nunes, A. Onofre, and A. Torres-Forné, Comparison of neural network architectures for feature extraction from binary black hole merger waveforms, arXiv e-prints , arXiv:2307.16668 (2023).
- [64] T. S. Yamamoto, S. Kuroyanagi, and G.-C. Liu, Deep learning for intermittent gravitational wave signals, *Phys. Rev. D* **107**, 044032 (2023).
- [65] D. Beveridge, L. Wen, and A. Wicencec, Detection of Binary Black Hole Mergers from the Signal-to-Noise Ratio Time Series Using Deep Learning, arXiv e-prints , arXiv:2308.08429 (2023).
- [66] S. Jadhav, M. Shrivastava, and S. Mitra, Towards a robust and reliable deep learning approach for detection of compact binary mergers in gravitational wave data, *Machine Learning: Science and Technology* **4**, 045028 (2023).
- [67] Q. Tang, N. Yang, and J. Li, Deep learning for parameter estimation of supermassive binary black holes with simulated LISA data, *Chinese Journal of Physics* **88**, 301 (2024).
- [68] E. Marx, W. Benoit, A. Gunny, R. Omer, D. Chatterjee, R. C. Venterea, L. Wills, M. Saleem, E. Moreno, R. Raikman, E. Govorkova, D. Rankin, M. W. Coughlin, P. Harris, and E. Katsavounidis, A machine-learning pipeline for real-time detection of gravitational waves from compact binary coalescences, arXiv e-prints , arXiv:2403.18661 (2024).
- [69] S. Sasaoka, N. Koyama, D. Dominguez, Y. Sakai, K. Somiya, Y. Omae, and H. Takahashi, Comparative study of 1D and 2D convolutional neural network models with attribution analysis for gravitational wave detection from compact binary coalescences, *Phys. Rev. D* **109**, 043011 (2024).
- [70] O. Zelenka, B. Brüggmann, and F. Ohme, Convolutional Neural Networks for signal detection in real LIGO data, arXiv e-prints , arXiv:2402.07492 (2024).
- [71] A. Trovato, E. Chassande-Mottin, M. Bejger, R. Flamarly, and N. Courty, Neural network time-series classifiers for gravitational-wave searches in single-detector periods, *Classical and Quantum Gravity* **41**, 125003 (2024).
- [72] M. B. Schäfer, O. Zelenka, A. H. Nitz, H. Wang, S. Wu, Z.-K. Guo, Z. Cao, Z. Ren, P. Nousi, N. Stergioulas, P. Iosif, A. E. Koloniari, A. Tefas, N. Passalis, F. Salemi, G. Vedovato, S. Klimenko, T. Mishra, B. Brüggmann, E. Cuoco, E. A. Huerta, C. Messenger, and F. Ohme, MLGWSC-1: The first Machine Learning Gravitational-Wave Search Mock Data Challenge, arXiv e-prints , arXiv:2209.11146 (2022).
- [73] P. Nousi, A. E. Koloniari, N. Passalis, P. Iosif, N. Stergioulas, and A. Tefas, Deep residual networks for gravitational wave detection, *Phys. Rev. D* **108**, 024022 (2023).
- [74] *AResGW* code (2022), <https://github.com/vivinousi/gw-detection-deep-learning>.
- [75] R. Abbott *et al.* (KAGRA, VIRGO, LIGO Scientific), Open Data from the Third Observing Run of LIGO, Virgo, KAGRA, and GEO, *Astrophys. J. Suppl.* **267**, 29 (2023).
- [76] G. Pratten, C. García-Quirós, M. Colleoni, A. Ramos-Buades, H. Estellés, M. Mateu-Lucena, R. Jaume, M. Haney, D. Keitel, J. E. Thompson, and S. Husa, Computationally efficient models for the dominant and subdominant harmonic modes of precessing binary black holes, *Phys. Rev. D* **103**, 104056 (2021).
- [77] M. Zevin and Gravity Spy, Gravity Spy - Integrating LIGO detector characterization, citizen science, and machine learning, in *American Astronomical Society Meeting Abstracts #228*, American Astronomical Society Meeting Abstracts, Vol. 228 (2016) p. 109.02.
- [78] S. Soni, C. P. L. Berry, S. B. Coughlin, M. Harandi, C. B. Jackson, K. Crowston, C. Østerlund, O. Patane, A. K. Katsaggelos, L. Trouille, V. G. Baranowski, W. F. Domainko, K. Kaminski, M. A. L. Rodriguez, U. Marciniak, P. Nauta, G. Niklasch, R. R. Rote, B. Téglás, C. Unsworth, and C. Zhang, Discovering features in gravitational-wave data through detector characterization, citizen science and machine learning, *Classical and Quantum Gravity* **38**, 195016 (2021).
- [79] J. Glanzer, S. Banagiri, S. B. Coughlin, S. Soni, M. Zevin, C. P. L. Berry, O. Patane, S. Bahaadini, N. Rohani, K. Crowston, V. Kalogera, C. Østerlund, L. Trouille, and A. Katsaggelos, Data quality up to the third observing run of advanced LIGO: Gravity Spy glitch classifications, *Classical and Quantum Gravity* **40**, 065004 (2023).
- [80] M. Zevin, C. B. Jackson, Z. Doctor, Y. Wu, C. Østerlund, L. C. Johnson, C. P. L. Berry, K. Crowston, S. B. Coughlin, V. Kalogera, S. Banagiri, D. Davis, J. Glanzer, R. Hao, A. K. Katsaggelos, O. Patane, J. Sanchez, J. Smith, S. Soni, L. Trouille, M. Walker, I. Aerith, W. Domainko, V.-G. Baranowski, G. Niklasch, and B. Téglás, Gravity Spy: lessons learned

- and a path forward, *European Physical Journal Plus* **139**, 100 (2024).
- [81] Gravity spy machine learning classifications of ligo glitches from observing run o3a and o3b (2021), <https://zenodo.org/records/5649212>.
- [82] F. Robinet, N. Arnaud, N. Leroy, A. Lundgren, D. Macleod, and J. McIver, Omicron: A tool to characterize transient noise in gravitational-wave detectors, *SoftwareX* **12**, 100620 (2020).
- [83] G. Ashton, M. Hübner, P. D. Lasky, C. Talbot, K. Ackley, S. Biscoveanu, Q. Chu, A. Divakarla, P. J. Easter, B. Goncharov, F. Hernandez Vivanco, J. Harms, M. E. Lower, G. D. Meadors, D. Melchor, E. Payne, M. D. Pitkin, J. Powell, N. Sarin, R. J. E. Smith, and E. Thrane, BILBY: A User-friendly Bayesian Inference Library for Gravitational-wave Astronomy, *ApJS* **241**, 27 (2019).
- [84] Planck Collaboration, Planck 2015 results. XIII. Cosmological parameters, *Astron. Astrophys.* **594**, A13 (2016).
- [85] J. S. Speagle, DYNESTY: a dynamic nested sampling package for estimating Bayesian posteriors and evidences, *MNRAS* **493**, 3132 (2020).
- [86] M. Hannam, P. Schmidt, A. Bohé, L. Haegel, S. Husa, F. Ohme, G. Pratten, and M. Pürrer, Simple Model of Complete Precessing Black-Hole-Binary Gravitational Waveforms, *Phys. Rev. Lett.* **113**, 151101 (2014).
- [87] S. A. Usman, A. H. Nitz, I. W. Harry, C. M. Biwer, D. A. Brown, M. Cabero, C. D. Capano, T. Dal Canton, T. Dent, S. Fairhurst, *et al.*, The pycbc search for gravitational waves from compact binary coalescence, *Classical and Quantum Gravity* **33**, 215004 (2016).
- [88] L. S. Collaboration and V. Collaboration, A guide to LIGO-Virgo detector noise and extraction of transient gravitational-wave signals, *Classical and Quantum Gravity* **37**, 055002 (2020).
- [89] B. Allen, χ^2 time-frequency discriminator for gravitational wave detection, *Phys. Rev. D* **71**, 062001 (2005).
- [90] LIGO Scientific Collaboration and Virgo Collaboration, GW150914: First results from the search for binary black hole coalescence with Advanced LIGO, *Phys. Rev. D* **93**, 122003 (2016).
- [91] F. Aubin, F. Brighenti, R. Chierici, D. Estevez, G. Greco, G. M. Guidi, V. Juste, F. Marion, B. Mours, E. Nitoglia, O. Sauter, and V. Sordini, The MBTA pipeline for detecting compact binary coalescences in the third LIGO-Virgo observing run, *Classical and Quantum Gravity* **38**, 095004 (2021).
- [92] W. M. Farr, J. R. Gair, I. Mandel, and C. Cutler, Counting and confusion: Bayesian rate estimation with multiple populations, *Phys. Rev. D* **91**, 023005 (2015).
- [93] L. S. Collaboration, V. Collaboration, and K. Collaboration, Gwtc-3: Compact binary coalescences observed by ligo and virgo during the second part of the third observing run — o3 search sensitivity estimates (2021).
- [94] B. P. Abbott *et al.* (LIGO Scientific, Virgo), Binary Black Hole Mergers in the first Advanced LIGO Observing Run, *Phys. Rev. X* **6**, 041015 (2016), [Erratum: *Phys.Rev.X* 8, 039903 (2018)].
- [95] A. Virtuoso and E. Milotti, Wavelet-based tools to analyze, filter, and reconstruct transient gravitational-wave signals, *Phys. Rev. D* **109**, 102010 (2024).
- [96] A. Virtuoso and E. Milotti, Wavelet-based tools to analyze, filter, and reconstruct transient gravitational-wave signals / code release (1.0) (2024).
- [97] V. Tiwari and S. Fairhurst, The Emergence of Structure in the Binary Black Hole Mass Distribution, *Astrophys. J. Lett.* **913**, L19 (2021).
- [98] F. R. N. Schneider, P. Podsiadlowski, and E. Laplace, Bimodal Black Hole Mass Distribution and Chirp Masses of Binary Black Hole Mergers, *Astrophys. J. Lett.* **950**, L9 (2023).
- [99] M. Fishbach, D. E. Holz, and W. M. Farr, Does the Black Hole Merger Rate Evolve with Redshift?, *Astrophys. J. Lett.* **863**, L41 (2018).
- [100] S. Biscoveanu, T. A. Callister, C.-J. Haster, K. K. Y. Ng, S. Vitale, and W. M. Farr, The Binary Black Hole Spin Distribution Likely Broadens with Redshift, *Astrophys. J. Lett.* **932**, L19 (2022).